

The GLEAM 4-Jy (G4Jy) Sample: IV. Multiwavelength data and analysis

Sarah V. White^{1,2,3*}, Precious K. Sejake⁴, Kshitij Thorat⁴, Heinz Andernach^{5,6}, Thomas M.O. Franzen⁷, O. Ivy Wong^{8,9}, Anna D. Kapińska¹⁰, Joseph R. Callingham^{11,12}, Christopher J. Riseley^{13,14}, Nick Seymour³, Randall Wayth¹⁵, Lister Staveley–Smith⁹, Rajan Chhetri³, Natasha Hurley-Walker³, John Morgan³, Paul Hancock³, Francesco Massaro^{16,17,18}, Abigail García–Pérez^{16,19,20}, Ana Jiménez–Gallardo²⁰, and Harold A. Peña–Herazo²¹

¹South African Astronomical Observatory (SAAO), PO Box 9, Observatory, 7935, South Africa

²Department of Physics and Electronics, Rhodes University, PO Box 94, Grahamstown, 6140, South Africa

³International Centre for Radio Astronomy Research (ICRAR), Curtin University, Bentley, WA 6102, Australia

⁴Department of Physics, University of Pretoria, Hatfield, Pretoria, 0028, South Africa

⁵Thüringer Landessternwarte, Sternwarte 5, D-07778 Tautenburg, Germany

⁶Permanent address: Depto. de Astronomía, DCNE, Univ. de Guanajuato, Callejón de Jalisco s/n, C.P. 36023 Guanajuato, Mexico

⁷Square Kilometre Array Observatory (SKAO), Jodrell Bank, Lower Withington, Macclesfield, SK11 9FT, UK

⁸CSIRO Space & Astronomy, PO Box 1130, Bentley, WA 6102, Australia

⁹ICRAR, University of Western Australia (M468), 35 Stirling Highway, Crawley, WA 6009, Australia

¹⁰National Radio Astronomy Observatory (NRAO), 1003 Lopezville Rd, Socorro NM 87801, USA

¹¹Netherlands Institute for Radio Astronomy (ASTRON), Oude Hoogeveensedijk 4, 7991 PD, Dwingeloo, The Netherlands

¹²Anton Pannekoek Institute for Astronomy, University of Amsterdam, Science Park 904, 1098 XH, Amsterdam, The Netherlands

¹³Astronomisches Institut, Ruhr-Universität Bochum Universitätsstraße 150, 44801 Bochum, Germany

¹⁴Ruhr Astroparticle and Plasma Physics Center (RAPP Center), 44780 Bochum, Germany

¹⁵SKAO, 26 Dick Perry Ave, Kensington, WA 6151, Australia

¹⁶Dipartimento di Fisica, Università degli Studi di Torino, via Pietro Giuria 1, I-10125 Torino, Italy

¹⁷Istituto Nazionale di Astrofisica (INAF) - Osservatorio Astrofisico di Torino, via Osservatorio 20, 10025 Pino Torinese, Italy

¹⁸Istituto Nazionale di Fisica Nucleare (INFN) - Sezione di Torino, via Pietro Giuria 1, I-10125 Torino, Italy

¹⁹Instituto Nacional de Astrofísica, Óptica y Electrónica, Luis Enrique Erro 1, Tonantzintla, Puebla 72840, México

²⁰European Southern Observatory (ESO), Alonso de Córdova 3107, Vitacura, Región Metropolitana, Chile

²¹East Asian Observatory (EAO), 660 N. A'ohōkū Place, Hilo, HI 96720, USA

Accepted 2026 March 4. Received 2026 February 7; in original form 2025 August 8

ABSTRACT

We provide an updated ‘multiwavelength’ version of the G4Jy catalogue (available at <https://github.com/svw26/G4Jy>, <https://zenodo.org/communities/g4jy/records>, and through VizierR), which has 127 new host-galaxy identifications, as described in Paper III of this paper series. We also supplement the redshift information ($0.0 < z < 3.6$), gathered in Paper III, with *griz* photometry available through DR10 of the DESI Legacy Surveys. Together, this legacy dataset allows us to investigate the multiwavelength properties of these southern radio-bright galaxies, which includes an initial analysis of radio spectral-curvature for this complete sample ($S_{151\text{MHz}} > 4\text{Jy}$). For example, we present (for the first time in the literature) the radio-power–size diagram as a function of radio spectral-curvature, $[P-D]$ (SCI), noting that the spectral-curvature index (SCI) can act as a proxy for the spectral age of the radio source. This radio-power–size–age diagram shows a predominance of radio galaxies with $\text{SCI} > 0.15$ and $D < 200\text{kpc}$, which are candidates for both remnant radio-galaxies and young radio-sources, and a vast range of linear sizes for candidate restarted radio-galaxies (having $\text{SCI} < -0.15$). We also show that (i) G4Jy sources populate the entirety of *WISE* colour-colour space, (ii) optically point-like sources (i.e. candidate quasars) are brighter than the well-studied $K-z$ relation (as expected), and (iii) there is no relation between the SCI of the radio source and its host-galaxy properties.

Key words: galaxies: active – galaxies: evolution – galaxies: high-redshift – radio continuum: galaxies – catalogues

1 INTRODUCTION

It is now well-established that at the centre of every galaxy is a supermassive black-hole (e.g. Ryle & Longair 1967; Richstone et al. 1998; Event Horizon Telescope Collaboration et al. 2019; Do et al. 2019), with galaxies forming and growing in a hierarchical fash-

* sarahwhite.astro@gmail.com

ion (e.g. Toomre & Toomre 1972; Rocca-Volmerange & Guiderdoni 1990; White & Frenk 1991; Kauffmann & Charlot 1998). If there is accretion of material onto the black hole, resulting in emission that supplements that of the host galaxy, we describe the galaxy as being ‘active’ and the central region as being an ‘active galactic nucleus’ (AGN; see the review by Antonucci 1993, and references therein).

AGN are assumed to be axisymmetric and, as such, their appearance (i.e. observed properties) depend upon the angle with which we view them (e.g. Lawrence & Elvis 1982; Urry & Padovani 1995). Therefore, it is vital that we study them at multiple wavelengths, in order to build up a more-cohesive picture regarding the physical processes that take place in these exciting sources. For example, relevant for radiatively-efficient AGN, the accretion disc is visible in the optical when viewing the AGN \sim face-on, and gives rise to the broad-line and narrow-line regions through photoionisation (e.g. Pogge 1988). However, the putative dusty ‘torus’ (e.g. Pier & Krolik 1992) that surrounds the accretion disc will block the innermost optical light if the source is viewed edge-on. Meanwhile, that same warm/hot dust re-radiates in the mid-infrared, allowing both dust-obscured and dust-unobscured AGN to be detected (Wright et al. 2010; Stern et al. 2012). Similarly, the far-infrared allows us to probe the cooler dust that is heated by star-formation processes in the host galaxy (e.g. Smith et al. 2012), and so is direction-independent (e.g. Sanders et al. 1989). The downside is that far-infrared observations are biased towards high star-formation rates, with dust mass being degenerate with dust temperature (Dunne et al. 2000; Dunne & Eales 2001; da Cunha et al. 2010).

Ultimately, we want to understand how physical processes affect the evolution of galaxies. This could be the way in which AGN activity affects star formation, and so either promoting (e.g. Ishibashi & Fabian 2012; Silk 2013) or suppressing (e.g. Croton et al. 2006; Davies et al. 2020; Lammers et al. 2023) the growth of the host galaxy. A key advantage of radio observations is that they are sensitive to *both* AGN activity and star-formation processes (e.g. White et al. 2015, 2017; White 2023), independent of the amount of dust along the line-of-sight (e.g. De Breuck et al. 2000; Collier et al. 2014; Singh et al. 2014). They therefore give us a more-complete census of galaxy-evolution processes across cosmic time (e.g. Madau & Dickinson 2014; McAlpine et al. 2015).

However, studies of the radio properties of AGN are typically conducted at mid/high radio-frequencies ($\gtrsim 1$ GHz), where radio cores, jets, and hotspots are subject to relativistic beaming (Rees 1966). This leads to a bias in the orientation of the jet axis with respect to the line-of-sight (e.g. Lister 2003), and likely impacts upon the conclusions that we draw from population studies. Like the revised Third Cambridge Catalogue of Radio Sources (3CRR; Laing et al. 1983), the G4Jy Sample (White et al. 2018, 2020a,b) does not suffer from this bias, due to its selection at low radio-frequencies ($S_{151\text{MHz}} > 4\text{Jy}$). This is because low-frequency radio emission is dominated by the radio lobes (see the review by Hardcastle & Croston 2020), which do not exhibit beaming effects and therefore provide a more ‘isotropic’ view of AGN (Barthel 1989). Furthermore, the fact that low radio-frequencies allow the cumulative effect of AGN activity to be probed over longer timescales (e.g. Kardashev 1962; Pacholczyk 1970; Jaffe & Perola 1973) means that we can build a better understanding of the variety in AGN life-cycles (e.g. Harwood et al. 2013; Turner & Shabala 2015; Shabala et al. 2020) compared with studies restricted to mid/high frequencies. This is because the latter are biased towards to more-recent AGN (or star-formation) activity.

However, the radio continuum does not have characteristic spectral features that allow the redshift of the source to be derived (e.g.

Condon 1992), and so it is vital to combine radio-continuum datasets with information at other wavelengths (or radio spectral-line information, where possible) in order to draw scientific conclusions (e.g. Mauch & Sadler 2007; Best & Heckman 2012; Franzen et al. 2021). For example, Sabater et al. (2019) and Dabhade et al. (2020) have combined the first data release of the LOFAR Two-metre Sky Survey (LoTSS DR1; Shimwell et al. 2019; Williams et al. 2019) with optical spectroscopy from the Sloan Digital Sky Survey (SDSS; York et al. 2000; Abazajian et al. 2009) in order to study local radio-detected AGN and identify giant radio-galaxies (GRGs), respectively. Sabater et al. (2019) find that the most massive galaxies have AGN that are always ‘switched on’, and Dabhade et al. (2020) show that their sample of 239 GRGs have spectral indices like those of ‘normal-sized’ radio-galaxies. Both results prompt us to more-carefully consider the ‘duty cycle’ of the AGN, and how these sources interact with their environment (e.g. Hardcastle & Krause 2013, 2014).

We know that AGN must exhibit a ‘duty cycle’ (which is the ratio of the time it spends in an ‘on’ state to the time it spends in an ‘off’/quiescent state) because several sources show restarted AGN activity. For example, Schoenmakers et al. (2000) identified ‘double-double’ radio galaxies where the outer pair of radio lobes is the result of old AGN activity, whilst the inner pair of radio lobes is the result of more-recent activity. A more-unusual case of recurrent activity is that of G4Jy 1080 (IC 4296), where past activity has carved out a pair of tunnels in the surrounding medium, which are then filled with plasma that reaches equilibrium (Condon et al. 2021). At a later time, a new set of jets appear in the same direction as the tunnels, as evidenced via the MeerKAT intensity-map and accompanying spectral-index map (noting that flatter radio emission indicates compact, ongoing activity associated with e.g. the radio core).

Equally important are so-called ‘remnant radio-galaxies’, where the radio core is *not* detected and the only sign of AGN activity is the past emission in the form of radio lobes (e.g. Murgia et al. 2011; Mahatma et al. 2018; Quici et al. 2021). This importance is because, as shown by theoretical models (e.g. Turner 2018; Turner et al. 2023), a complete sample is needed in order to understand the relative proportions of different types of radio galaxy, and so constrain the typical lifecycle for the full population (e.g. Shabala et al. 2020). These models are aided by spectral-curvature information (as suggested by Turner et al. 2018), and so, clearly, a multifrequency view is required to understand the entire lifecycle of AGN.

Thankfully, help is at hand with the excellent spectral coverage that is provided by the Murchison Widefield Array (MWA; Tingay et al. 2013), through the GaLactic and Extragalactic All-sky MWA (GLEAM; Wayth et al. 2015) Survey (i.e. 20 flux-density measurements at 72 to 231 MHz). The G4Jy Sample was constructed from this low-frequency survey, and will allow models of powerful AGN to be tested more robustly than previously (e.g. Mullin et al. 2008; Wang & Kaiser 2008; Turner & Shabala 2015).

1.1 Paper outline

This is the fourth paper in the G4Jy paper series, and is outlined as follows: Section 2 describes the multiwavelength datasets that we consider for our multiwavelength analysis, further to the redshift information collated for Paper III. This is followed by additional detailing of the multiwavelength G4Jy catalogue in Section 3. We then present and discuss the results of studying the radio, mid-infrared, and near-infrared properties of G4Jy sources in Section 4. Our conclusions are described in Section 5, the G4Jy-catalogue metadata are provided in Appendix A, additional figures are presented in Appendix B, and giant radio-galaxies are discussed in Appendix C.

J2000 co-ordinates and AB magnitudes are used throughout this work, except where *WISE* magnitudes are considered (e.g. Section 2.2) – these are in the Vega system. We apply a Λ CDM cosmology, with $H_0 = 70 \text{ km s}^{-1} \text{ Mpc}^{-1}$, $\Omega_m = 0.3$, $\Omega_\Lambda = 0.7$.

2 DATA

Whilst work towards the ‘multiwavelength’ G4Jy catalogue is based on numerous datasets, in this section we only describe those that are of direct relevance for the multiwavelength analysis that is presented in this paper. For example, the newest dataset that we consider is the tenth data release of the DESI Legacy (Imaging) Surveys (Dey et al. 2019), which is summarised in Section 2.4. For further details of the radio data, we refer the reader to Papers I, II, and III.

2.1 Radio data

The multi-frequency coverage provided by the MWA (Tingay et al. 2013) enables excellent low-frequency constraints of radio emission, with 20 flux-density measurements (from 72 MHz to 231 MHz) provided through the GLEAM Survey (Wayth et al. 2015). The 151-MHz sub-band flux-density was used to search for, and select, radio sources with a total, integrated $S_{151 \text{ MHz}}$ greater than 4 Jy, thereby creating the G4Jy Sample (White et al. 2020a,b). These radio sources are distributed across the southern sky (Dec. $< +30$ deg, $|b| > 10$ deg), following the footprint of the GLEAM Extragalactic Catalogue (Hurley-Walker et al. 2017). The details of individual GLEAM components are provided in the original G4Jy catalogue (White et al. 2020a,b) – including the GLEAM components that required re-fitting – whilst the total, integrated flux-densities for the 20 sub-bands are retained for the updated ‘multiwavelength’ G4Jy catalogue.

The two G4Jy catalogues can easily be combined via cross-matching on the radio-centroid positions. These were calculated by White et al. (2020a,b) via the imaging and catalogues provided by (i) the Sydney University Molonglo Sky Survey (SUMSS; Mauch et al. 2003; Murphy et al. 2007) at 843 MHz, and (ii) the NRAO (National Radio Astronomy Observatory) VLA (Very Large Array) Sky Survey (NVSS; Condon et al. 1998) at 1.4 GHz. Both surveys have a spatial resolution of ~ 45 arcsec, which allowed White et al. (2020a,b) to (a) visually assess the radio morphology of G4Jy sources (‘single’, ‘double’, ‘triple’, ‘complex’), and (b) estimate their angular sizes, as consistently as possible.

White et al. (2020a,b) also recorded the total flux-densities measured via SUMSS- and NVSS-catalogue data (see section 5.2 of Paper III), and from these measurements, they derived two-point spectral indices (G4Jy_SUMSS_alpha = $\alpha_{151 \text{ MHz}}^{843 \text{ MHz}}$, and G4Jy_NVSS_alpha = $\alpha_{151 \text{ MHz}}^{1400 \text{ MHz}}$), following an assumed power-law description of the radio emission ($S_\nu \propto \nu^\alpha$). Such an assumption was also made when calculating the 20-point, low-frequency spectral-index, G4Jy_alpha = $\alpha_{72 \text{ MHz}}^{231 \text{ MHz}}$ (based upon the total, integrated flux-densities provided in the G4Jy catalogue). For reference, the $5\text{-}\sigma$ surface-brightness limits of the relevant surveys (GLEAM, SUMSS, and NVSS) are $S_{200 \text{ MHz}} \gtrsim 50 \text{ mJy beam}^{-1}$, $S_{843 \text{ MHz}} \approx 6\text{--}10 \text{ mJy beam}^{-1}$, and $S_{1400 \text{ MHz}} \approx 2.5 \text{ mJy beam}^{-1}$, respectively.

For the current work, we also refer to MeerKAT and VLASS (VLA Sky Survey; Lacy et al. 2020) radio-images, which are made available to the community by Sejake et al. (2023), Gordon et al. (2020), and Dong et al., in prep. These images have a spatial resolution of ~ 7 arcsec and ~ 2.5 arcsec, respectively, and we use them to obtain more-accurate angular-sizes for bonafide giant radio-galaxies (Ta-

ble C1). However, as in Paper III, we note that updating the angular sizes in the G4Jy catalogue is deferred to future work.

2.2 Mid-infrared data

In Papers II (White et al. 2020a) and III (White et al. 2026), we (predominantly) identified the host galaxy of G4Jy sources in AllWISE-W1 mid-infrared images (Cutri et al. 2013) in order to avoid the bias incurred by dust-obscuration (which affects optical surveys). This band is at $3.4 \mu\text{m}$, and is accompanied by bands W2 ($4.6 \mu\text{m}$), W3 ($12 \mu\text{m}$), and W4 ($22 \mu\text{m}$), courtesy of the *Wide-field Infrared Survey Explorer* (WISE; Wright et al. 2010). The all-sky survey conducted with WISE resulted in $5\text{-}\sigma$ sensitivities of 0.054, 0.071, 0.73, and 5.0 mJy, respectively, at the following corresponding resolutions: 6.1, 6.4, 6.5, and 12.0 arcsec. In terms of signal-to-noise ratios (SNRs), we find that six sources in the G4Jy Sample have $\text{SNR} < 5$ for the W1 band. These are G4Jy 573, G4Jy 764, G4Jy 1299, G4Jy 1312, G4Jy 1341, and G4Jy 1576, due to being either very mid-infrared faint or affected by nearby bright mid-infrared emission. In addition, we quote the AllWISE measurements as (Vega) magnitudes, noting that the $>95\text{-per-cent}$ completeness levels are 17.1, 15.7, 11.5, and 7.7 mag in W1, W2, W3 and W4, respectively (Cutri et al. 2013)¹.

2.3 Near-infrared data

Magnitudes are presented in the G4Jy catalogue for the near-infrared bands, J , H , and K_s , from the Two Micron All-Sky Survey (2MASS; Cutri et al. 2003; Skrutskie et al. 2006) via the AllWISE catalogue. These observations are from two 1.3-m telescopes, located at Cerro Tololo in Chile and Mount Hopkins in Arizona, and dedicated to the survey. The result is \sim all-sky coverage to the following $10\text{-}\sigma$ depths, with apertures of 4-arcsec radius: $J = 15.8$, $H = 15.1$, and $K_s = 14.3$ mag (in the Vega-magnitude system). The resolution of the imaging is 2.5 arcsec – this being the result of 2 arcsec pixel⁻¹ detectors, the instrument response, and the best seeing conditions – and the astrometric accuracy is of the order 100 mas. 2MASS constructed a Point-Source Catalogue of 470,992,970 sources, and an Extended Source Catalogue (Jarrett et al. 2000) containing 1,647,599 sources. G4Jy sources that have their host galaxy identified in the 2MASS Extended Source Catalogue are denoted with the prefix of ‘2MASX’.

2.4 Optical photometry

We turn to Data Release 10 (DR10) of the DESI Legacy (Imaging) Surveys (Dey et al. 2019) for optical photometry in the g , r , i and z bands. These data have been obtained through the Beijing–Arizona Sky Survey (BASS; Zou et al. 2017) and the Mayall z -band Legacy Survey (MzLS; Silva et al. 2016) for sources above a Declination of 32.375 deg, and through the Dark Energy Camera (DECam; Flaugher et al. 2015) Legacy Survey (DECaLS) for sources below this Declination². For homogeneity, LEGACYPIPE³ software has been run to perform all of the steps from calibrating images to creating catalogues. It includes the running of SOURCEEXTRACTOR (Bertin & Arnouts 1996) and PSFEX (Bertin 2011) to generate light-profile models, which are then passed to an algorithm called THE TRACTOR (Lang et al. 2016)

¹ https://wise2.ipac.caltech.edu/docs/release/allwise/expsup/sec2_1.html

² A reminder that the entirety of the G4Jy Sample is at Dec. < 30.0 deg.

³ <https://github.com/legacysurvey/legacypipe>

for model-fitting and photometry. The $5\text{-}\sigma$ AB-magnitude depths reached are $g = 24.0$, $r = 23.4$, and $z = 22.5$ mag (Dey et al. 2019), and the 50th-percentile depths⁴ are $g = 24.9$, $r = 24.4$, $i = 24.0$, and $z = 23.4$ mag. Meanwhile, the astrometric precision is better than ± 0.03 arcsec. This is having used the epoch of a given Legacy Surveys observation to predict *GAIA* (Global Astrometric Interferometer for Astrophysics; Lindegren et al. 1994) positions to which certain source positions are tied. In doing so, the source extraction becomes fixed to the *GAIA* Data Release 2 (Gaia Collaboration et al. 2018) system. For details of the information that is retained for the G4Jy catalogue, see Section 3.1.

2.5 Optical spectroscopy

In Paper III we described the multiple optical-spectroscopy datasets that we have gathered, assessed, and re-fitted (where necessary) for the G4Jy Sample, with the aim of reaching 100 per cent spectroscopic completeness. This is crucial for taking full advantage of the lack of bias in the low-frequency selection of the sources, and so allowing the most-robust comparisons with theoretical models. We list these spectroscopy datasets in table 2 of White et al. (2026) and, as a result of this thorough work, the G4Jy Sample currently has a spectroscopic completeness of 34 per cent and a redshift range of $0.00075 < z < 3.56990$.

3 THE G4JY MULTIWAVELENGTH CATALOGUE

The original G4Jy catalogue provided detailed information for the low-frequency radio emission of all 1,863 G4Jy sources, as well as mid-infrared data through 1,606 host-galaxy identifications in AllWISE (which itself is accompanied by near-infrared data from 2MASS). Thanks to supplementary work on identifying the host galaxies of the radio emission (described in Paper III), we now have a total of 1,733 identifications for collating additional multiwavelength information (this section) and conducting further analysis (Section 4).

3.1 Crossmatching photometry

We obtain optical photometry (Section 2.4) through a crossmatch of the G4Jy catalogue with the Legacy Surveys DR10 (Dey et al. 2019). This is performed on the host-galaxy positions (given by `host_RAJ2000`, `host_DEJ2000`) with a radius of 1 arcsec, to be conservative. This is because 1 arcsec is the typical resolution of the VISTA Hemisphere Survey DR5 (McMahon et al. 2021) imaging, within which 17 of the G4Jy sources were identified. (Note that the prefix of the `host_name` gives an indication of the method/data through which a particular source was identified.)

The Legacy Surveys DR10 provides a wealth of information for the southern sky⁵, and the columns that are retained for our purposes are listed in Table A1 (Appendix A). This includes the optical morphological type⁶ (labelled ‘`morphtype_LSDR10`’ in the G4Jy catalogue; see Table 1), and we direct the reader to Section 4.2.1 for how we use this in combination with *WISE* colour-colour space. In addition

Table 1. The optical morphology types that are fitted by THE TRACTOR (Lang et al. 2016) as part of photometric-catalogue creation for the DESI Legacy Surveys (Dey et al. 2019). The ‘Fitting’ column indicates whether the Sérsic index for that particular morphology type is fixed or is allowed to vary, and ‘0’ is a placeholder value in the ‘Sérsic index’ column for ‘PSF’ sources. These results are crossmatched into the G4Jy catalogue (Appendix A) via a matching radius of 1 arcsec on the host-galaxy positions (Section 3.1).

Morph. type	Description of the optical light profile	Sérsic index	Fitting
PSF	Point-spread function (for point-sources)	0	fixed
EXP	Exponential disc (for spiral galaxies)	1	fixed
REX	Round exponential of variable radius	1	fixed
DEV	de Vaucouleurs (1948) $r^{-1/4}$ power-law	4	fixed
SER	Sérsic (1963) light profile	0.5 to 6.0	varies

to the *griz* magnitudes are ‘de-reddened’ magnitudes for these optical bands, which have been determined through fitting for Galactic extinction. We also retain information regarding the signal-to-noise per optical band, the size of the point-spread function (PSF), and the Sérsic index that is determined alongside the optical morphology (Table 1).

We note that G4Jy names are now fully resolvable in many online databases, and this includes the Legacy Surveys Sky Viewer⁷. Visual inspection of optical images for the full G4Jy Sample is beyond the scope of the current work, but is planned for the future as part of aiding spectroscopic follow-up (particularly for the optically-fainter sources, at $r > 20$ mag).

3.2 Redshift information

Within the G4Jy catalogue, spectroscopic redshifts can be found in the ‘`zsp_misc`’ column, photometric redshifts can be found in the ‘`zph_misc`’ column, and redshifts data-mined via NED⁸ can be found in the ‘`z_NED`’ column. In determining a single `z_origin_flag` per source (see table 2 of Paper III), the available redshifts have the following order of preference: `zsp_misc` > `zph_misc` > `z_NED`. Later in this paper we refer to ‘cumulative redshifts’, by which we mean we have a single redshift per source ($z = z_{sp}$ or z_{ph} or z_{NED}), following the aforementioned order of redshift preference.

Our spectroscopic-redshift assessment (Paper III) included visually inspecting the available spectroscopy and assigning a ‘`z_Quality_flag`’, *Q*. A reminder of the meanings of the different quality flags are repeated here for convenience:

- *Q* = 1 indicates that the redshift is highly robust, with multiple spectral features detected with good signal-to-noise ratios. This flag is also assigned when a single *broad* emission-line⁹ (with a distinctive profile, e.g. Ly- α) is detected with very good signal-to-noise.
- *Q* = 2 indicates that the redshift is fairly robust, where multiple spectral features are detected but they are less discernible from the continuum or noise level than for *Q* = 1.
- *Q* = 3 indicates that the redshift is a tentative measurement,

⁴ These values were made available through the Astro Data Lab User Forum, <https://datalab.noirlab.edu/help/> – thank you!

⁵ <https://www.legacysurvey.org/dr10/files/#tractor-catalogs-south-tractor>

⁶ <https://www.legacysurvey.org/dr10/description/#morphological-classification>

⁷ For example, G4Jy 1080 can be viewed via <https://www.legacysurvey.org/viewer/#G4Jy%201080>

⁸ <https://ned.ipac.caltech.edu>

⁹ We caution that a single narrow ‘line’ may be the result of a cosmic ray being detected, or poor background-subtraction near detector-chip edges.

as suggested by the marginal detection of multiple spectral features against the continuum/noise.

- $Q = 4$ indicates that the redshift is unreliable, as it is derived from (a) a single spectral feature detected with low-to-moderate signal-to-noise, (b) one or more spectral features that have been misidentified (resulting in an incorrect redshift calculation), or (c) spectral features that are not discernible by eye.

- $Q = 5$ indicates that visual inspection of the spectroscopy has not been completed (e.g. because the spectrum is not available online). This flag is automatically given to all photometric redshifts and all redshifts acquired through automated data-mining of the NASA/IPAC Extragalactic Database (NED).

If there are multiple spectroscopic redshifts available for a given source, the one with the lowest Q value (i.e. the best quality) is retained for the G4Jy catalogue. Our ultimate aim is for 100 per cent of the sample to have spectroscopic redshifts where $Q = 1$ or 2.

For interest, we retain the spectroscopic redshifts provided by the DESI Collaboration et al. (2025) as a separate column, ‘zsp_DESI’. Alongside this is the warning flag¹⁰ (‘zsp_WARN_DESI’), which is ‘0’ for all DESI-covered sources except: G4Jy 178, G4Jy 227, G4Jy 1165, and G4Jy 1228. For these, the warning flag is ‘4’, which means that there are many outliers in terms of redshift-template fitting. However, following our visual inspection (Paper III), we believe that zsp_WARN_DESI = 4 may be overcautious for G4Jy 227, since we have assigned it a z_Quality_flag of 1.

Similarly, we retain the main columns from the photometric catalogues, WISExSuperCOSMOS (wiseScos; Bilicki et al. 2016) and DESI LS DR8 photo-z South (LSDR8south; Duncan 2022), for the G4Jy catalogue. Please see Appendix A for confirmation of these.

3.3 Radio data per GLEAM component

The parent catalogue for the G4Jy Sample is the GLEAM Extragalactic Catalogue (Hurley-Walker et al. 2017), which provides detailed characterisation of low-frequency radio-emission on a component-by-component basis (subject to ~ 2 -arcmin spatial resolution via the MWA Phase-I beam). GLEAM components could describe an entire radio-source or an individual radio-lobe (or part thereof), hence the additional work that is needed to create *source* catalogues, such as the G4Jy catalogue (White et al. 2020a,b). For the latter we retained information for the 1,960 GLEAM components that correspond to 1,863 G4Jy sources (including 15 components that were re-fitted), and introduced a G4Jy_component column to enable a short-hand way of referring to a particular GLEAM-component. For example, G4Jy 7A is GLEAM J000441+124907 and G4Jy 7B is GLEAM J000456+124810, both belonging to the source, G4Jy 7.

To simplify the combining of the G4Jy catalogue with other datasets, we hereafter refer to G4Jy sources as opposed to constituent GLEAM components. (This avoids repeating source properties, such as redshift, across multiple rows for multi-GLEAM-component sources.) As such, only the total, integrated flux-densities (per GLEAM sub-band) and spectral indices are retained for the latest G4Jy catalogue. If the reader would like to combine both the original and the updated G4Jy catalogues, they can do so easily by cross-matching on the radio-centroid positions (White et al. 2020a,b). This will then allow them to access the wealth of low-frequency information that is listed in appendix E of Paper

I, such as the local noise-level (Jy beam^{-1}) in the 72–80 MHz sub-band image per GLEAM component.

3.4 Ancillary information

Accompanying the redshifts from NED are: alternative names of G4Jy sources in published work, the fiducial R.A. and Dec. quoted in NED, and the source ‘type’¹¹ (e.g. ‘RadioS’ for radio source) that corresponds to the alternative name. Furthermore, the descriptions for columns that are newly-added to form the G4Jy multiwavelength catalogue can be found in Appendix A.

4 RESULTS AND DISCUSSION

In this section we consider the multiwavelength properties of the G4Jy Sample, and incorporate the newly-acquired redshifts (White et al. 2025, 2026) into this analysis. We start with analysis of the spectral curvature that is exhibited through the radio emission at multiple frequencies (Section 4.1.1), which will be explored further in a future paper (White et al., in prep.). Each of the subsequent sub-sections then connects back to this spectral analysis, which itself is enabled by the excellent low-frequency coverage provided by the MWA, through the GLEAM survey.

4.1 Radio properties

4.1.1 Spectral curvature

Previously, White et al. (2020b) presented the radio spectra for 67 G4Jy sources that overlap with the 3CRR sample (Laing et al. 1983), G4Jy-3CRR, by way of assessing the flux-density scale (see their table 8 and appendix F). These spectra, like those of Laing & Peacock (1980), demonstrate that the bright radio emission from these sources does *not* always follow the power-law function ($S_\nu \propto \nu^\alpha$, where α is the spectral index) that is typically assumed to describe the radio emission. Of course, this is already evident from the presence of peaked-spectrum sources (e.g. Callingham et al. 2017), which are believed to be radio sources in the early stages of their lifetimes. Nevertheless, we often construct two-point spectral indices (i.e. α values that are constrained by flux-densities at two different frequencies) as a simple way of extrapolating measured flux-densities from one frequency to another. This is the purpose intended for the G4Jy_NVSS_alpha (G4Jy_SUMSS_alpha) values provided in the G4Jy catalogue, which are calculated between 151 MHz and 1400 MHz (843 MHz, respectively) and aid, for example, follow-up observations with MeerKAT (Sejake et al. 2023).

Also provided in the G4Jy catalogue is the integrated spectral-index, G4Jy_alpha, through (power-law) fitting to all 20 flux-densities within the GLEAM band, which spans 72 to 231 MHz. Accompanied by a reduced- χ^2 value for the fitting, the availability of this spectral index indicates the validity of the low-frequency emission being approximated by $S_\nu \propto \nu^\alpha$. [Please see White et al. (2020b) for further details.] Therefore, we can assess the degree of spectral curvature *beyond* this frequency range by comparing G4Jy_alpha with G4Jy_NVSS_alpha and G4Jy_SUMSS_alpha (Figure 1ab). If a power-law description remains an accurate approximation, then the two values will equal each other, with the resulting datapoint lying

¹⁰ <https://desidatamodel.readthedocs.io/en/latest/bitmasks.html#zwarn>

¹¹ <https://ned.ipac.caltech.edu/help/ui/nearposn-list-objecttypes>

on the 1:1 relation (diagonal dashed-lines) in Figure 1. Sources lying above the 1:1 relation have a radio spectrum that can be described as ‘concave’, whilst sources lying below the 1:1 relation have a radio spectrum that can be described as ‘convex’ (with respect to the frequency axis).

Note that there are subtle differences in the distributions of G4Jy_NVSS_alpha and G4Jy_SUMSS_alpha [see figure 14a of White et al. (2020b)], on account of the higher-frequency end being different (i.e. 1400 MHz and 843 MHz, respectively). Coupled with the fact that sources lie at different redshifts, this means that different rest-frame frequencies are being probed. Until we have direct measurements of the whole sample at 1400 MHz, we only consider the spectral curvature for sources that are at Dec. > -39.5 deg, and are therefore covered by the NVSS footprint. This equates to 77 per cent of the G4Jy Sample, with their spectral indices presented again in Figure 1c.

Whilst the vast majority of sources show steep-spectrum emission ($\alpha < -0.5$), the number of sources lying above the 1:1 relation exceeds the number of sources lying below the 1:1 relation. In the case of G4Jy-NVSS sources, this unevenness in the distribution is quantified by 27 per cent of the subsample lying below the line (Figure 1a). The corresponding percentage for G4Jy-SUMSS sources is 13 per cent (Figure 1b). We also note that sources above the line, where the low-frequency emission is steeper than the mid-frequency emission, could represent examples of restarted radio-galaxies, in agreement with simulations by Turner (2018). These simulations also show that the mid-frequency emission is steeper than the low-frequency emission, as one would expect, for ageing radio-galaxies (lying below the 1:1 relation). Therefore, the distribution in spectral curvature allows for constraints to be placed on the lifecycles of a complete AGN sample.

Next, we split the datapoints for NVSS sources (Figure 1a) into five regions in $\alpha_{\text{low}} - \alpha_{\text{mid}}$ space (Figure 1c), with these categorised spectral-curvature values being of interest for the remainder of the multiwavelength analysis described in this section. Formally, we define the spectral-curvature index (SCI) as:

$$\text{SCI}_0 = \alpha_{\text{low}} - \alpha_{\text{mid}}. \quad (1)$$

Whilst this may appear to be the opposite way round from the definition put forward by Murgia et al. (2011), the sense in which they define a power-law is also opposite to our definition: $S_\nu \propto \nu^{-\alpha}$. The result is that we have the same physical interpretation of the spectral-curvature-index values, these being $\text{SCI}_0 < -0.05$ for candidate restarted/renewed radio-galaxies, and $\text{SCI}_0 > 0.05$ for candidate ageing/remnant radio-galaxies (Figure 1d). [We emphasise our use of the word ‘candidate’ to describe these categories, since further analysis (beyond the scope of this work) is needed to determine, e.g., the true fraction of remnant radio-galaxies.] The $-0.05 < \text{SCI}_0 < 0.05$ interval represents the G4Jy sources that have radio emission that is typically well-described by a power-law function from 72 MHz to 1400 MHz, as also indicated by coincidence with the 1:1 relation. For the median spectral-curvature indices (and median spectral-indices) for the five intervals, please see Table 2, noting that the typical uncertainty in the SCI_0 value is 0.02.

We note that sources with very old radio-emission, and no signs of recent activity in the radio, should occupy the region defined by $\text{SCI}_0 > 0.15$ (though not exclusively). That is, this is the parameter space within which we expect to find remnant radio-galaxies (Murgia et al. 2011; Mahatma et al. 2018; Quici et al. 2021, 2025, Stewart et al., in prep.), which could help (in part) to explain the earlier observation that there are fewer sources in the sample lying below the 1:1 relation. In other words, this may be a selection effect

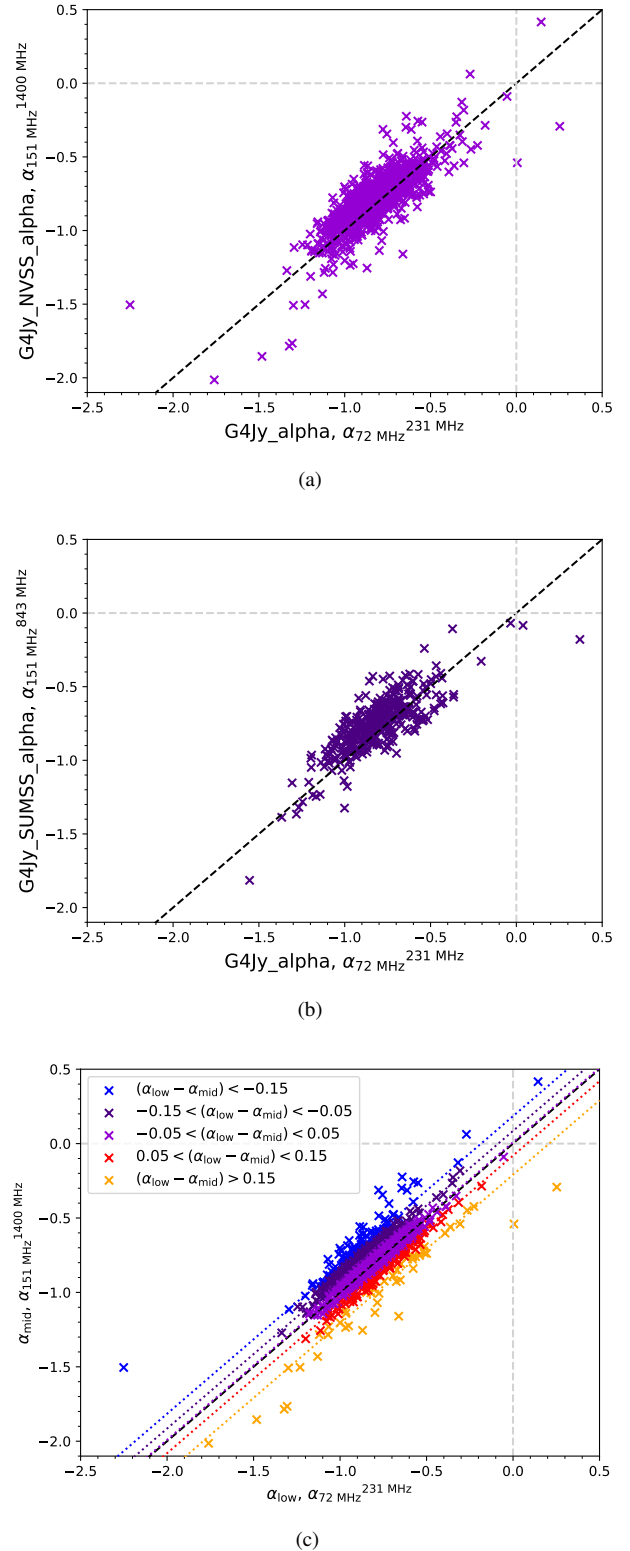


Figure 1. Distributions in the different spectral indices [G4Jy_alpha, (a) G4Jy_NVSS_alpha, and (b) G4Jy_SUMSS_alpha] that are available in the G4Jy catalogue. In each panel, a two-point spectral index (y-axis value) is plotted against the 20-point spectral index derived at low radio-frequencies, G4Jy_alpha (Section 4.1.1). The latter is renamed ‘ α_{low} ’ for panel (c), and each panel has a diagonal dashed-line that represents the 1:1 relation. For panel (c), the NVSS distribution is split into five regions of differing degrees of spectral curvature, as indicated by the $\alpha_{\text{low}} - \alpha_{\text{mid}}$ value in the legend. The diagonal dotted-lines (in blue, indigo, violet, red, and orange) represent the median $\alpha_{\text{low}} - \alpha_{\text{mid}}$ values (i.e. per region), which are provided in Table 2.

Spectral curvature index, $\alpha_{\text{low}} - \alpha_{\text{mid}}$	Median $\alpha_{\text{low}} - \alpha_{\text{mid}}$	Median α_{low}	Median α_{mid}
< -0.15	-0.184	-0.887	-0.702
-0.15 to -0.05	-0.085	-0.863	-0.777
-0.05 to 0.05	-0.009	-0.804	-0.798
0.05 to 0.15	0.081	-0.767	-0.842
> 0.15	0.209	-0.695	-0.927

Table 2. Median values in the spectral-curvature index, $\text{SCI}_0 = \alpha_{\text{low}} - \alpha_{\text{mid}}$ (Section 4.1.1), for five different regions of Figure 1c. For interest, we also provide the median in the low-frequency spectral-index (α_{low}) and the mid-frequency spectral-index (α_{mid}) for these intervals/regions.

connected to the identification completeness of the G4Jy Sample. The NVSS (and SUMSS flux-densities) are *integrated* values, and the spatial distribution of this mid-frequency emission could be such that the radio core is only marginally detected (e.g. G4Jy 1289; Sejake et al. 2023). As a result, the α_{mid} value will be much steeper than previously estimated, leading to a datapoint that moves towards the lower right-hand corner of the $\text{SCI}_0 = \alpha_{\text{low}} - \alpha_{\text{mid}}$ plane. Therefore, obtaining core flux-densities for the full sample, where possible, is the only way in which we can be sure that the remnant radio-galaxy population is properly constrained. [See Mahatma et al. (2018) for further discussion.]

Before progressing further with the discussion, we caution that the $\text{SCI}_0 > 0.05$ sources may include *young* radio-galaxies exhibiting a peaked spectrum. (I.e., spectral turnover of the radio emission results in a spectral shape that is flatter at lower frequencies than at higher frequencies.) Such a peaked spectrum is thought to be due to free-free absorption or synchrotron self-absorption processes in compact sources. This complicates the interpretation of the SCI_0 value as a proxy for the spectral age of the source, which is why we again emphasise that this category is described as *candidate* ageing/remnant radio-galaxies. The ratio of truly-ageing sources to young sources is currently unknown, but will be clarified by ongoing spectral-age analysis (White et al., in prep.). In the meantime, we note that 10 per cent of $\text{SCI}_0 > 0.05$ sources have $\alpha_{\text{low}} < -1.0$ – a combination that most-clearly can be interpreted as a dying radio-galaxy, and so acts as a lower limit. If we consider the $\text{SCI}_0 > 0.15$ subset, this fraction (of NVSS sources with $\alpha_{\text{low}} < -1.0$) increases to 21 per cent.

We also investigate whether there is a trend within the $\text{SCI}_0 = \alpha_{\text{low}} - \alpha_{\text{mid}}$ plane that is brought to light by a correlation with the spectroscopic redshift (Appendix B). However, no such trend is visible, which goes against the idea that following-up sources with ultra-steep spectral indices ($\alpha \lesssim -1.3$; De Breuck et al. 2000) is an effective way of identifying high-redshift sources (e.g. Blumenthal & Miley 1979; Roettgering et al. 1994; Saxena et al. 2018). This may be because, as suggested by Gopal-Krishna (1988), Onuora (1989) and Pinjarkar et al. (2025), the apparent connection between spectral index and redshift is rather driven by an underlying correlation between spectral index and radio luminosity (see also Sejake et al., submitted).

In addition, Figure 2 presents the redshift histograms for G4Jy-NVSS sources, as a function of spectral curvature (with spectroscopic redshifts resulting in the shaded histograms). Whilst (likely) restarted radio-galaxies have been found out to $z \sim 3$, the candidate remnant radio-galaxies [with $\text{SCI}_0 > 0.15$] are more-restricted in redshift range. This could be because host-galaxy identification is more difficult for remnant sources than the general population of radio galaxies (e.g. see Mahatma et al. 2018, and the discussion by Stewart et al., in

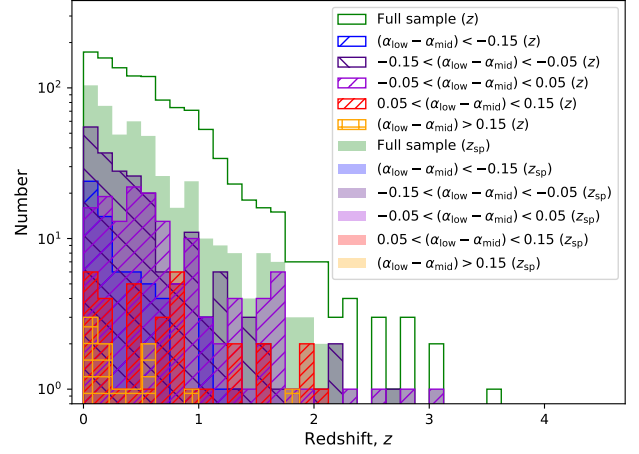


Figure 2. Distributions of the redshifts for G4Jy-NVSS sources, colour-coded by the degree of spectral curvature (Section 4.1.1). ‘Cumulative redshifts’ ($z = z_{\text{sp}}, z_{\text{ph}}, z_{\text{NED}}$) are used to determine the outlined histograms, and spectroscopic redshifts (z_{sp}) are used to determine the shaded histograms.

prep.), and becomes even more difficult with the fainter core radio-emission at higher redshifts. This is convolved with the difficulty in obtaining redshifts for optically-fainter sources, where the amount of dust and/or distance become limiting factors. Furthermore, for example, Godfrey et al. (2017) and Hardcastle (2018) suggest that the fraction of remnants is likely to be much lower at higher redshift due to a combination of observational (surface-brightness dimming) and physical (increased inverse-Compton losses) effects.

By way of concluding Section 4.1.1, we note that further broadband spectral analysis will be presented in G4Jy Paper V (White et al., in prep.).

4.1.2 Radio luminosities

In Paper III (figure 9) we presented the radio-luminosity– z distribution of G4Jy sources that have newly-collated redshifts in the updated G4Jy catalogue (Section 3). This showed that, as predicted, the lower flux-density threshold used to select the G4Jy Sample (White et al. 2020a,b), compared to 3CRR (Laing et al. 1983), allows both lower radio-luminosities and higher redshifts to be probed. This is important for future studies of the interplay of AGN activity and star formation in the host galaxy, with the large sample size also allowing environmental effects to be taken into consideration.

For this work, we present the radio luminosities of G4Jy-NVSS sources as a function of spectral curvature, SCI_0 , in Figure 3. This is a novel way of investigating the properties of the sources, but their luminosity distributions do not show any discernible trends. For example, we may have expected the (candidate) ‘restarted’ radio-galaxies (in blue) to show higher-than-average radio luminosities, but the actual distribution (Figure 3a) is a reminder that the *low*-frequency radio emission is tracing *older* populations of relativistic electrons. To see whether our expectation holds for 1400-MHz radio-luminosities, which tend to trace more-recent AGN activity, we plot the latter in Figure 3b. The only marginal trend that can be seen is the slightly greater clustering of $0.05 < \text{SCI}_0 < 0.15$ sources (in red) towards higher 1400-MHz luminosities. It is possible that this is connected to the relativistic beaming that is seen at higher radio-frequencies, but if that were the case then we would expect to see a similar effect for sources with more negative values of spectral

curvature. Remnant radio-galaxies are ‘exempt’ from this expectation because the 1400-MHz luminosity may still be confined to the unbeamed radio-lobes, as opposed to the beamed radio-core (itself depending on the orientation of the radio-jet axis with respect to the line-of-sight).

Of course, a complicating factor for all radio luminosities is the strength of the magnetic field within which the relativistic electrons (giving rise to the radio emission) are accelerating. We hope that such degeneracy will be addressed through X-ray observations of a complete, and statistically-large, radio-source (sub)sample.

4.1.3 Linear sizes

Again, as demonstrated in Paper III, the newly-acquired redshifts allow us to calculate the linear sizes of G4Jy sources. These are derived from angular sizes based on 45-arcsec imaging (see section 5.2 of Paper III), which may lead to overestimates of the extent of the radio emission. Such overestimation will affect small sources more greatly than larger sources, with projection effects further complicating the angular-size distribution.

For interest, we present the linear sizes as a function of spectral curvature (Figure 4). As with the corresponding radio-luminosity figure, we are able to discern few trends with respect to SCI_0 (Equation 1). One exception is that the (likely) oldest population (i.e. sources with $SCI_0 > 0.15$) have linear sizes below 600 kpc. This could be due to a scenario in which these sources happen to be more-confined by their environment (or growing more slowly) than is the case for the general population. Alternatively, it is the result of a selection effect, where more-extended radio emission (possibly from previous episodes of AGN activity) is beyond the sensitivity limit of the NVSS data, and so the linear size is underestimated. (As a reminder, only G4Jy sources within the NVSS footprint are considered, in terms of spectral curvature, because these have an α_{mid} value calculated between 151 and 1400 MHz.)

Consideration of which sources cross the 1-Mpc threshold to be categorised as giant radio galaxies (GRGs) is detailed in Appendix C.

4.1.4 P - D diagrams

In Figures 5 and 6 we present the 151-MHz radio-luminosity against the (projected) linear size. This parameter space is effectively a radio-power–size (P - D) diagram, as first constructed by Baldwin (1982) to help elucidate the evolutionary tracks of extended radio-galaxies. (See also Ryle & Longair 1967, and note that we have additionally plotted compact radio-galaxies in our figures, for completeness.) It is believed that radio galaxies traverse this P - D plane during their lifetime, expanding and brightening-then-fading as they do so, with starting points towards the left-hand side of the diagram and endpoints towards the right-hand side. The shape of their path is governed by the jet power and the environment into which the radio emission is expanding, which themselves are complicating factors (given the variety of jets and environments that we witness in radio-galaxy populations; e.g. Vardoulaki et al. 2024).

Another complication is estimating how quickly hotspots advance through the intergalactic medium (e.g. Alexander & Leahy 1987; An & Baan 2012; Stewart et al. 2025). However, this is only relevant for sources with FR-II morphology, and so simulations have been extended to incorporate the necessary physics for modelling FR-I radio-galaxies in addition (e.g. Turner 2018; Turner et al. 2023). This includes the difference in spectral signatures of the lobes of FR-Is and FR-IIs, caused by the different directions in which the shock-accelerated particles flow from the flare point. (That is, ‘forwards’

for FR-I sources and ‘backwards’ for FR-II sources.) We note that the viewing angle of the source will also have an impact on the spectral signature, with radio-jets close to the line-of-sight having their (high-frequency) flux-densities Doppler boosted, resulting in a flatter-than-average radio spectrum. This is less of a concern for the G4Jy Sample, since the low-frequency selection of these sources results in a sample that is unbiased with respect to the orientation of the radio-jet axis (Barthel 1989).

Despite all of these complex factors, the P - D diagram offers an informative way of exploring the radio-loud AGN population in further detail (e.g. see the model tracks in figure 8 of Hardcastle et al. 2019). The G4Jy Sample has a similar spread in radio luminosities (Figure 3) and linear sizes (Figure 4) as the 3CRR sample (Laing et al. 1983), and we now draw attention to the correspondence of different radio morphologies (White et al. 2020a,b) to different regions of P - D space (Figure 5).

Firstly, we note that the ‘complex’ label was assigned by White et al. (2020a,b) to sources with unusual morphologies (usually in cluster environments) but also to head-tail radio-galaxies and narrow-angle tailed radio-galaxies (whose morphologies are believed to have formed from the relative motion of the source through the cluster medium – see Paper II for examples). These sources tend to have lower radio-luminosities than the ‘doubles’ in our sample, and they occupy the lower left-hand region of P - D space. This suggests that the stability and density of the surrounding medium may restrict their distribution to small linear sizes. However, we know that ‘complex’ morphology can be maintained on large scales (e.g. Jaffe & Perola 1973), meaning that the small extents of ‘complex’ G4Jy sources is more-likely a selection effect (imposed by the surface-brightness limit of the radio imaging that is involved).

Meanwhile, the distribution of ‘complex’ sources appears to be in agreement with the work of Chilufya et al. (2025), who also study the P - D diagram as a function of radio morphology. They use the 2.5-arcsec resolution provided by VLASS to help with visual inspection of extended radio galaxies (>60 arcsec) detected in LoTSS DR2 (Shimwell et al. 2022). Their wide-angle tail, narrow-angle tail, head-tail, and relaxed-double radio-sources all occupy the same region of P - D space as our ‘complex’ sources, as do their radio galaxies showing typical FR-I and FR-II morphologies. Interestingly, this region is dominated by LERGs (see figure 7 of Chilufya et al. 2025), although this is likely influenced by selection effects – notably their restriction to $z < 0.57$ – since LERGs tend to dominate the radio-galaxy population at low redshifts (Best & Heckman 2012).

Quite striking is the distribution in P - D space of the sources with ‘single’ morphology (Figure 5), which (unfortunately) are not considered for the sample of Chilufya et al. (2025). These can generally be divided into two groups: firstly, the compact/point-like radio-sources that follow a trunk-like distribution. This can be explained by: (i) noting that the linear sizes for many of these sources are upper limits, given the spatial resolution of the radio data. (It is worthwhile comparing Figure 5 with figure 7 of White et al. 2025.) (ii), these may be sources whose radio jets have become ‘frustrated’ by the surrounding medium, slowing their maturation into (more-familiar) extended radio-galaxies. This is particularly relevant for short-lived compact symmetric objects (CSOs), as discussed by An & Baan (2012). Secondly, there are ‘single’ sources that are distributed more sparsely across a range of linear sizes, and even passing the commonly-used 700-kpc threshold (e.g. see Saripalli et al. 2005) for being classed as a GRG. These are sources that exhibit typical ‘core-brightened’, FR-I-like radio morphology, and FR-II sources that are not spatially resolved in NVSS/SUMSS. This is confirmed in higher-resolution

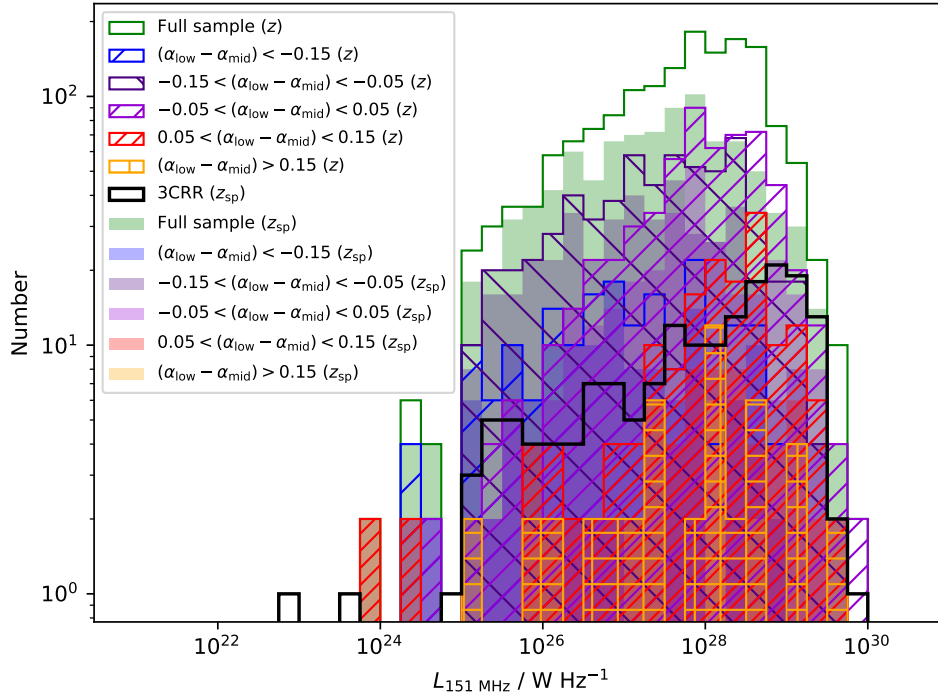
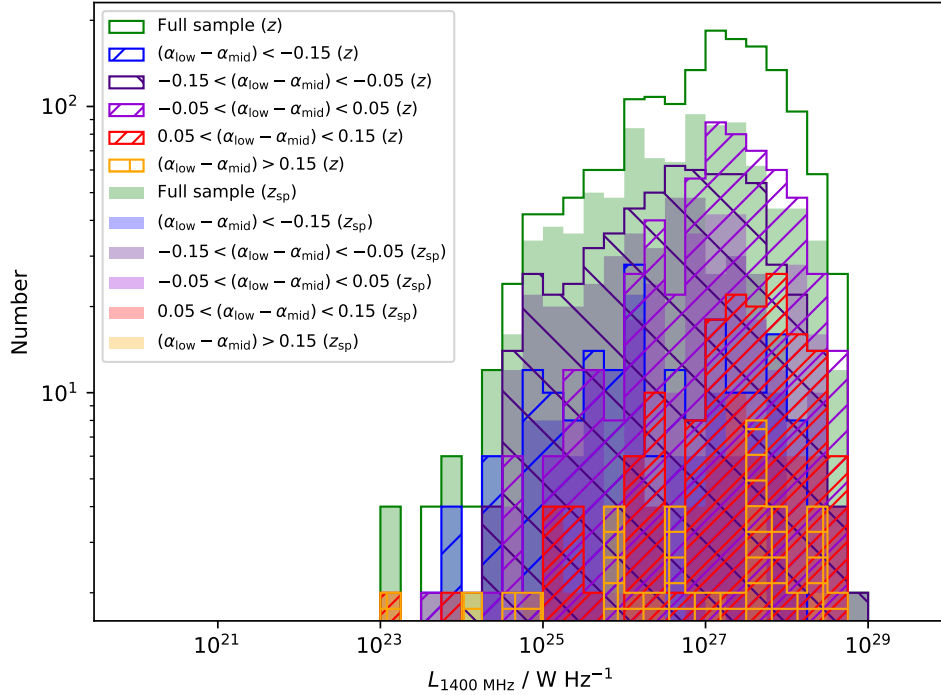

 (a) Radio luminosities of G4Jy-NVSS sources at 151 MHz, by spectral curvature (SCI_0)

 (b) Radio luminosities of G4Jy-NVSS sources at 1400 MHz, by spectral curvature (SCI_0)

Figure 3. Distributions in the radio luminosities at (a) 151 MHz, and (b) 1400 MHz (Section 4.1.2), colour-coded by the (radio) spectral curvature of the source (Section 4.1.1). The luminosity distribution for 3CRR sources (Laing et al. 1983) is added (to panel a) for comparison (black, unfilled histogram). In addition, ‘cumulative redshifts’ ($z = z_{sp}, z_{ph}, z_{NED}$) are used for the outlined histograms, whilst the shaded histograms are based on only the z_{sp} values being used for the luminosity calculation.

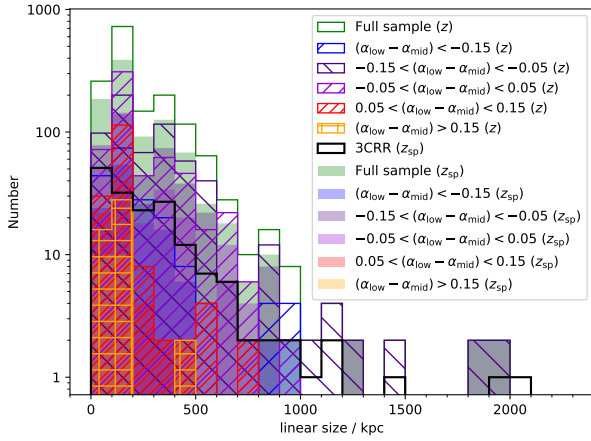
(a) Linear sizes by spectral curvature (SCI_0)

Figure 4. Distributions in the linear sizes of G4Jy-NVSS sources (Section 4.1.3), colour-coded by the spectral curvature index, $SCI_0 = \alpha_{low} - \alpha_{mid}$ (Section 4.1.1). The size distribution for 3CRR sources (Laing et al. 1983) is added for comparison (black histogram), with one source (3C 236) having a linear size that is beyond the plot range (at 4530 kpc). The outlined histograms represent linear sizes calculated from the ‘cumulative redshifts’ ($z = z_{sp}, z_{ph}, z_{NED}$), whilst the shaded histograms represent linear sizes calculated from spectroscopic redshifts alone (z_{sp}).

radio images from MeerKAT (Sejake et al. 2023) and VLASS (Dong et al., in prep.).

Naturally, ‘edge-brightened’ FR-II sources fall most easily into the ‘double’ category, and they span the largest range in P – D space (Figure 5, see also figure 6 of Chilufya et al. 2025). This suggests that a combination of jet power and environmental conditions have promoted their growth, with lifespans that are long enough that these sources may demonstrate renewed activity (Stewart et al., in prep.). The same can be said for sources with ‘triple’ morphology, although there is a slight clustering of these sources in the same region as the ‘complex’ sources. This could again be due to selection effects: for their ‘triple’ morphology to be distinguished they most likely are at lower redshift, where Malmquist bias means that they are also likely to have lower radio luminosities than the general population. This should be investigated further with higher-resolution radio images for the full sample. This selection effect is also evident in Figure 6a, where we see the expected trend between luminosity and redshift.

In addition, interpretation of the distribution of radio galaxies in the P – D diagram is complicated by the infrequently-studied strength of the magnetic fields within which the relativistic electrons are accelerating (e.g. Miley 1980; Jamrozy et al. 2004; Ineson et al. 2017). This will influence both the intrinsic jet-power and the path of the radio jets through the surrounding medium (Hardcastle & Krause 2014). To the best of our knowledge, how magnetic fields may contribute to slowing the radio jets to small spatial scales is yet to be investigated for a complete AGN sample. However, this could help to explain the distribution of (candidate) ageing radio-sources ($SCI_0 > 0.05$) in Figure 6b (which is the first time that the P – D diagram has been studied as a function of spectral curvature). Whilst some candidate remnant radio-galaxies can be seen towards the right-hand side of the plane, where evolutionary-track ‘endpoints’ lie, there is a predominance of these sources below ~ 200 kpc. This could represent a typical spatial scale beyond which these sources are less able to penetrate the circumgalactic medium and transition into more-extended radio-galaxies (e.g. Turner et al. 2023, Stewart et al., in prep.). When we have better radio-morphology information, it

would be interesting to see whether there is a correspondence between the FR-I/FR-II morphologies and their distribution in $[P$ – $D](SCI_0)$ space. However, the caveat mentioned in Section 4.1.1 remains: the small linear sizes of $SCI_0 > 0.05$ radio galaxies may be due to the young age of the source, where not enough time has passed for the radio jets to have travelled larger distances.

The fates of compact symmetric objects (CSOs) could also hold the key to understanding the predominance of (candidate) ageing radio-sources with linear sizes below ~ 200 kpc. As explained by An & Baan (2012), CSOs are observed as either the young stage of all radio sources (some of which expand into FR-I/FR-II morphologies), or are the endpoints of sources whose radio-jets were unable to propagate beyond the boundary between the interstellar medium (ISM) and the intergalactic medium (IGM). The typical length scales for such sources are on the order of 0.001–1 kpc (An & Baan 2012, see their figure 1), where the “short-lived central source activity results in flow instabilities before the ISM–IGM transition point, and the eventual dissipation of the lobe structure”.

Furthermore, by considering the unfilled symbols in Figure 6b, we can interpret the slight positive correlation between luminosity and size (for this ‘limb’ of $SCI_0 > 0.05$ sources) as upper limits imposed by the spatial resolution of the NVSS imaging. By obtaining more-accurate angular-sizes (and thereby linear sizes) for the full sample, the region where 3CRR sources are visible in the top left-hand corner of the P – D diagram will also be populated by G4Jy sources. This is relevant for FR-I sources in general, whose angular sizes may have been severely mis-estimated through the relatively poor brightness-sensitivity of NVSS compared to, e.g., MeerKAT. Further work (beyond the scope of this paper) would also help to determine the significance of projection effects on the linear-size distribution of the ageing radio-sources.

We also note the unusual prevalence of large radio-galaxies showing spectra that flatten at mid-frequencies ($SCI_0 < -0.05$). This is indicative of renewed AGN activity, with these sources possibly having expanded for so long that their duty cycle has been completed (i.e. these AGN are returning to their ‘on’ state; e.g. see figure 1 of Stewart et al. 2025). They may also have a predisposition for being located ‘in the field’ (allowing for less-constrained expansion than in e.g. clusters), with more-massive-than-average gas reservoirs that enable the AGN to be reignited more-easily. Moreover, spectral flattening at higher radio-frequencies is seen in simulations by Yates-Jones et al. (2022) for large radio-galaxies at high redshifts (see their figure 14). In this case, such spectral shape arises as a result of the low-frequency component, associated with the lobes, appearing faint (largely due to inverse-Compton losses) and moving to even lower radio-frequencies (*below* 151 MHz). Meanwhile, the mid-frequency emission associated with the core, jets, and hotspots remains prominent. This will be explored further in future work.

As suggested by White et al. (2025), X-ray and polarimetric follow-up observations could allow the degeneracy of some of the complicating factors (mentioned above) to be broken, enabling easier interpretation of the P – D diagram. Of course, this would also need to be accompanied by theoretical modelling, in order to understand the physics that underpins the evolution of different types of radio galaxy. Furthermore, after obtaining stellar masses for the G4Jy Sample, we will be able to test whether the steep radio spectral-curvature of more-compact sources corresponds to the ‘cross-over’ (Wilde et al. 2023) between the circumgalactic medium and the intergalactic medium.

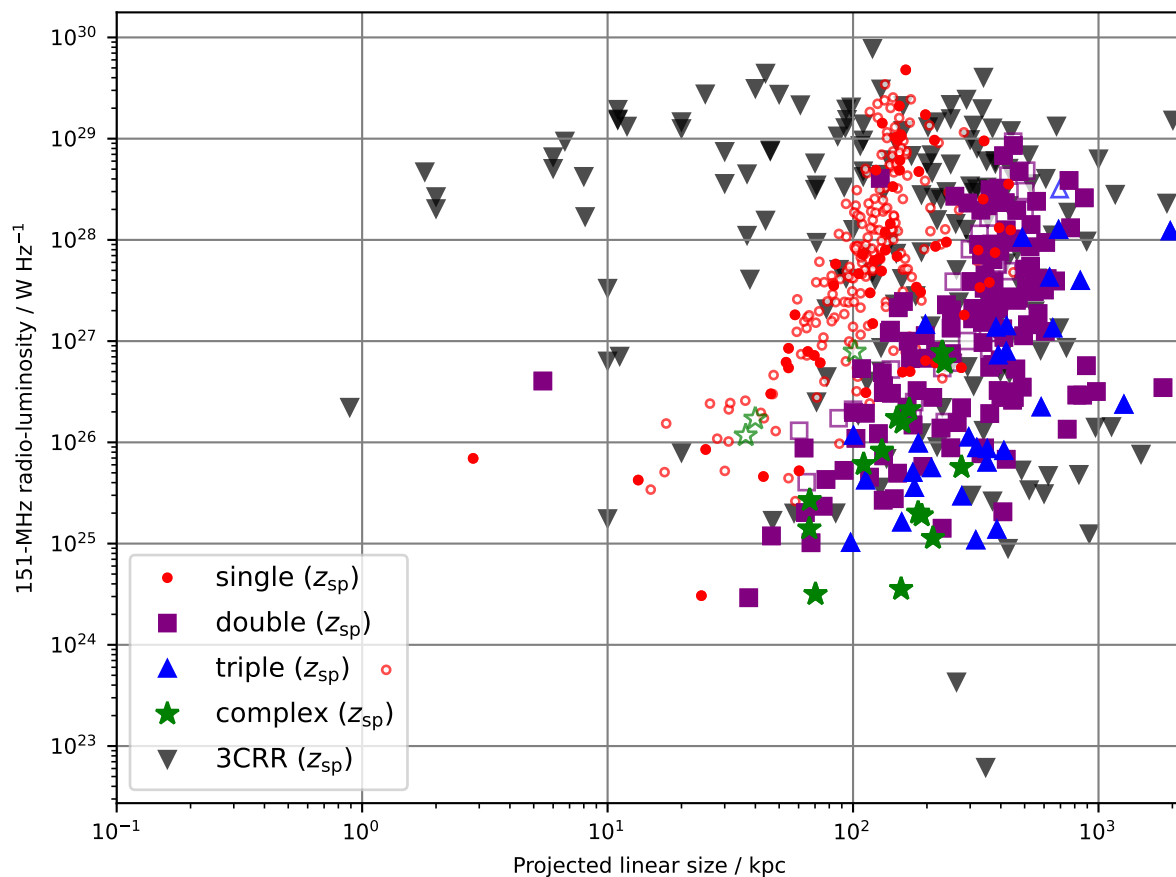


Figure 5. The P – D diagram (Baldwin 1982) for the G4Jy Sample (Section 4.1.4), thanks to newly-acquired spectroscopic redshifts for 34 per cent of the sample (White et al. 2025, 2026). Datapoints are colour-coded by the radio morphology of the sources, as determined by White et al. (2020a,b) via visual inspection of NVSS/SUMSS imaging (of 45-arcsec resolution). Also plotted, as black triangles, are sources belonging to the 3CRR sample (Laing et al. 1983) for comparison (and as a visual aid). The higher-resolution radio-maps available for 3CRR sources explain the lower linear-sizes that they reach, compared to the G4Jy Sample. Unfilled symbols represent G4Jy sources for which the linear-size measurement (via 45-arcsec imaging) is an upper limit.

4.2 Mid-infrared properties

4.2.1 WISE colour-colour space

In this section we focus on *WISE* colour-colour space (e.g. Figure 7), which is constructed by plotting $W1-W2$ against $W2-W3$ (see Section 2.2; Wright et al. 2010; Jarrett et al. 2017). It has been demonstrated by Stern et al. (2012) that $W1-W2 > 0.8$ mag can be used as a diagnostic for identifying sources with a warm/hot dusty torus, which are typically found in radiatively-efficient AGN such as quasars. Meanwhile, increasing (i.e. redder) values of $W2-W3$ show a correlation with the rate of star formation in the host galaxy (Jarrett et al. 2017), with starbursts typically found in the bottom right-hand corner of this parameter space.

These delineations have led many authors to use mid-infrared colours to differentiate AGN from star-forming galaxies, but the distribution of the G4Jy Sample (for example; see also figure 3 of Gürkan et al. 2014 and figure 14 by Jarrett et al. 2017) across a wide range of different colour combinations shows that relying on such a method is unwise¹². This is because the vast majority of the

G4Jy Sample are *known* to be radio-loud AGN, with notable exceptions being two very nearby star-forming galaxies (close enough to have their 151-MHz flux-density passing the 4 Jy threshold) and a lensed galaxy (where the magnification has boosted both the AGN and star-formation components) – see White et al. (2020a) for further details. Nonetheless, we note that the AGN signature in our sample is based upon low-frequency radio-emission, which may have been generated on the order of ~ 100 Myr ago (Alexander & Leahy 1987; Stewart et al. 2025) if the AGN has since ‘switched off’. Therefore, the mid-infrared emission may provide insight into *more-recent* levels of AGN and star-formation activity, with the caveat that radiatively-inefficient AGN (low-excitation radio-galaxies; LERGs; Best & Heckman 2012) still populate the region where $W1-W2 < 0.8$ mag.

Considering the full G4Jy Sample where there is coverage in $W1$ and $W2$, the percentage of sources with $W1-W2 > 0.8$ mag is $(728/1693 =) 43$ per cent, illustrating the need for colours beyond this range to be considered for AGN-selection completeness. (Only one fewer source does not also have coverage in the $W3$ band, which

¹² Of course, the criteria used to select AGN are usually a balance between reliability (how do we minimise contamination from other types of source?)

and completeness (have all of the AGN been selected?), and so the path taken depends on the science goals. In their figure 6, Stern et al. (2012) demonstrate the tradeoff between reliability and completeness for the $W1-W2$ criterion.

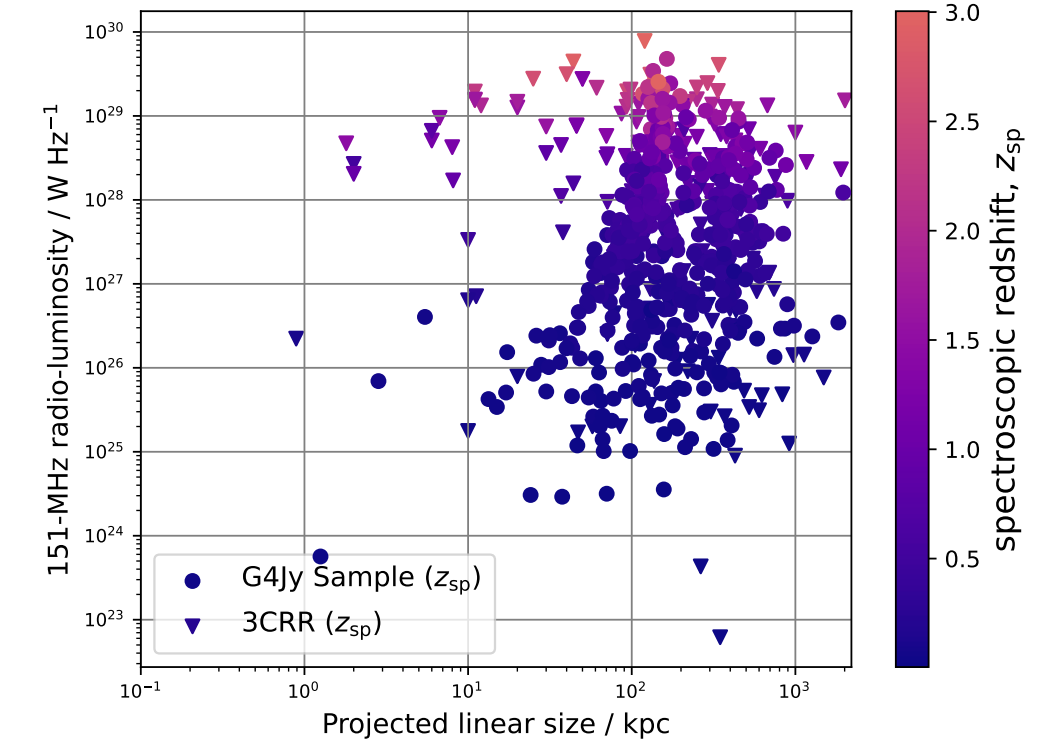
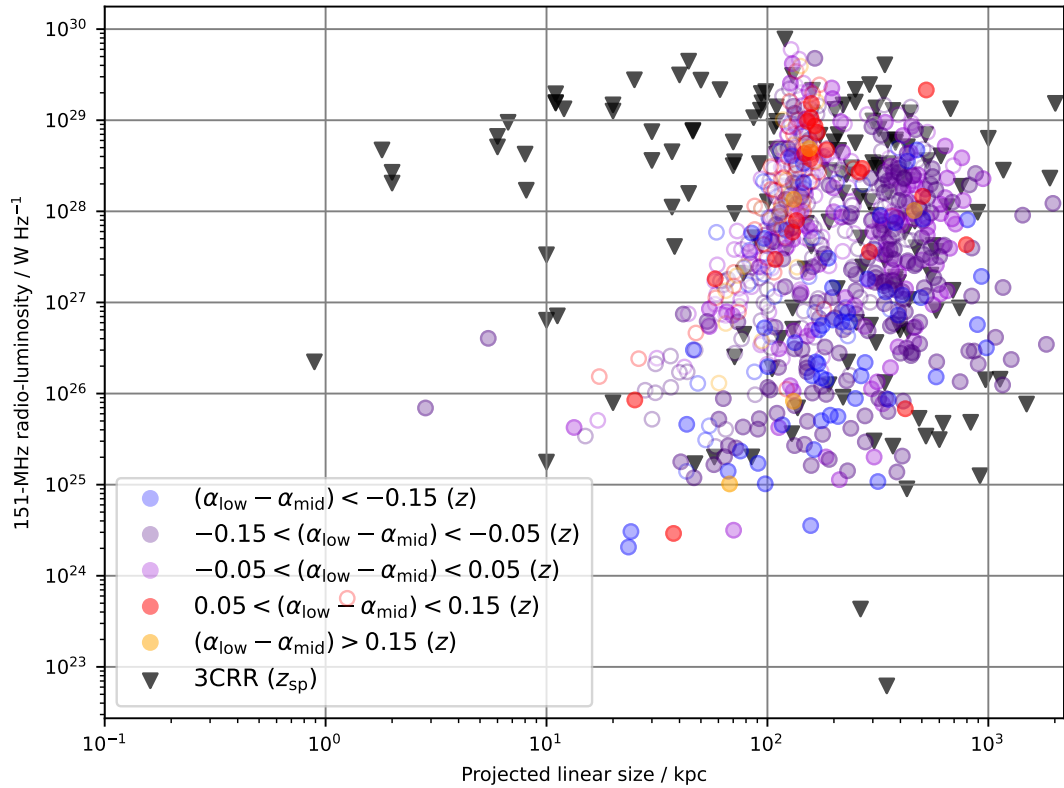
(a) P - D diagram colour-coded by z_{sp} (b) P - D diagram colour-coded by spectral curvature, SCI_0 (with unfilled symbols representing linear-size upper-limits)

Figure 6. P - D diagrams for G4Jy-NVSS sources (Section 4.1.4), where the 151-MHz radio luminosity (‘radio power’, P) is plotted against the linear size (D). The two panels are colour-coded by (a) spectroscopic redshift, and (b) spectral curvature, $SCI_0 = \alpha_{low} - \alpha_{mid}$ (Equation 1). The distribution for 3CRR sources (Laing et al. 1983) is added for comparison (triangles), with 3C 236 having a linear size that is beyond the plot range, at 4530 kpc. The number of sources is higher for panel (b), where z refers to the ‘cumulative redshifts’ (z_{sp} , z_{ph} , z_{NED}) that have been compiled for the sample, i.e. avoiding duplication of sources.

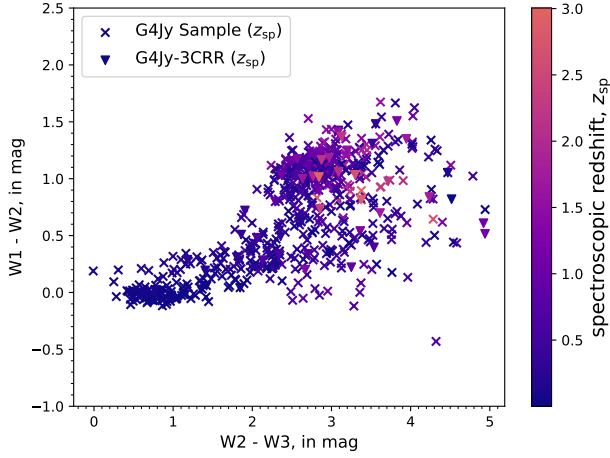


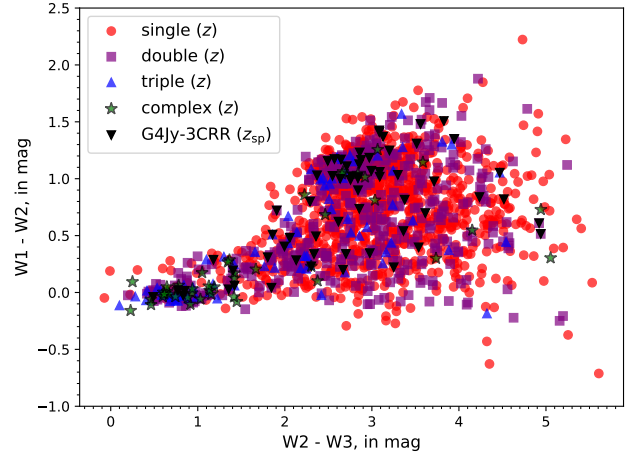
Figure 7. The *WISE* colour-colour diagram, with markers colour-coded by the spectroscopic redshift. ‘G4Jy-3CRR’ refers to the 67 3CRR sources (Laing et al. 1983) that overlap with the sample, as described by White et al. (2020b).

is of direct relevance for *WISE* colour-colour space.) Their median r -band magnitude is $r = 19.4$ mag, whilst the median r -band magnitude for sources with $W1 - W2 < 0.8$ mag is $r = 19.9$ mag. This is in good (qualitative) agreement with our initial spectroscopic follow-up (García-Pérez et al. 2024; White et al. 2025, Sejake et al., in prep.), which aims to achieve spectroscopic completeness to $r \sim 20$ mag.

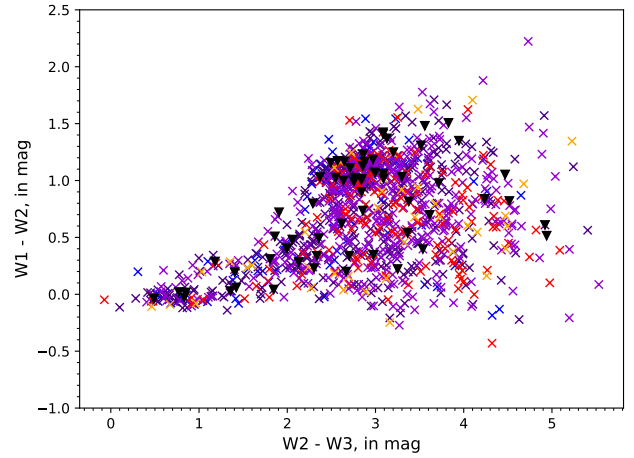
In Figure 7 we present the subset of the G4Jy Sample that has spectroscopic-redshift coverage. As expected, the highest redshifts are for the quasars (Wright et al. 2010), which are in the region defined by the $W1 - W2 > 0.8$ mag criterion of Stern et al. (2012). The robustness of this classification will be tested in future work, based on visual inspection of optical spectroscopy, and (in the meantime) we direct the interested reader to figure 7 of Sejake et al. (in prep.).

Next we consider the full G4Jy Sample, in Figure 8a, where the datapoints are colour-coded by radio morphology. The latter is based on the 45-arcsec imaging from NVSS/SUMSS, and 67 G4Jy-3CRR sources (White et al. 2020b) are added for reference. Now, without the criterion that the G4Jy source must have a spectroscopic redshift, we see better population of *WISE* colour-colour space. This is largely because optical spectroscopy is biased towards unobscured (Type-1) AGN, whereas the mid-infrared detects both unobscured and dust-obscured AGN very effectively (e.g. Stern et al. 2012). It could be argued that the ‘single’ radio morphology may be concealing additional star-forming galaxies in the sample, but sources with ‘double’ and ‘triple’ morphology are clearly AGN, and found throughout this mid-infrared parameter space.

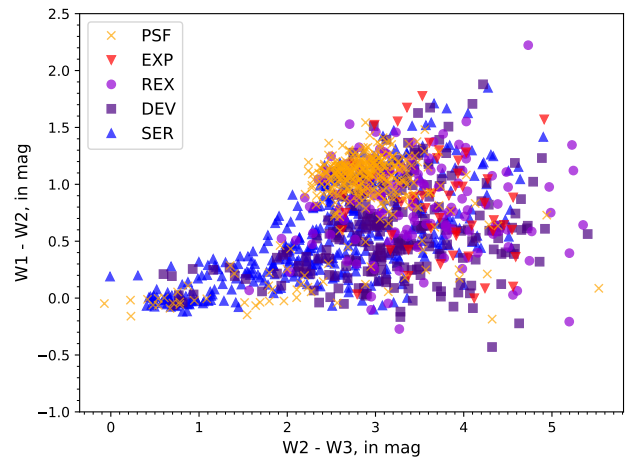
In Figure 8b we present the same colour-colour space, but for G4Jy-NVSS sources only (accounting for 77 per cent of the G4Jy Sample), and with markers colour-coded by the degree of spectral curvature (Equation 1). There appears to be no correlation between the spectral behaviour of the G4Jy sources and their *WISE* colours, which suggests a disconnect between the duty cycle of the AGN and the host galaxy. In other words, radio-loud AGN exhibit a wide range of lifespans, independent of their host-galaxy type. Another reason for the number of sources decreasing with respect to Figure 8a is that, whilst morphology information is available for the full sample, the calculation of SCI_0 depends on the 85-per-cent availability of a (power-law-fitted) G4Jy_alpha value. This restriction means that Figure 8b will be missing G4Jy sources that exhibit even greater de-



(a) *WISE* colour-colour space, by radio morphology



(b) *WISE* colour-colour space, by spectral curvature (SCI_0)



(c) *WISE* colour-colour space, by optical morphology

Figure 8. *WISE* colour-colour space (Section 4.2.1), with markers representing (a) different NVSS/SUMSS radio morphologies (White et al. 2020a,b), (b) different degrees of spectral curvature (Equation 1), and (c) the optical morphology of the source (classified via LSDR10; see Table 1). The legend for panel (b) is not shown for size reasons, but the colour-coding is the same as that for Figure 6b.

gresses of spectral curvature, and those sources will be studied further in G4Jy Paper V (White et al., in prep.).

We are also interested in the correspondence between the optical morphology (Table 1) and regions of *WISE* colour-colour space – see Figure 8c. This is most obvious for quasars, which are fitted by PSF light-profiles in the optical, and occupy a well-defined region in terms of mid-infrared colours. Again, the number of sources plotted has decreased (with respect to Figure 8a), this time due to the coverage provided by LSDR10 (Dey et al. 2019), which provides the optical-morphology classifications. We conclude with a note that the three orange (‘PSF’) crosses close to zero-zero in colour-colour space may actually be misidentified stars that have crept into our host-galaxy identification. These sources are G4Jy 21, G4Jy 636, and G4Jy 1843, and for the latter two, the G4Jy overlays suggest that the host is correct. (We propose MeerKAT follow-up to obtain a higher-resolution radio image for G4Jy 21.)

4.2.2 *W1-magnitude distributions*

For further interest, we present the *W1*-magnitude distribution for the G4Jy Sample in Figure 9, with the 67 3CRR sources that overlap with the sample showing a similar range in *W1* values. We also show the *W1* magnitudes for 55,731 radio galaxies in the (FIRST-based catalogue of the) first data release of Radio Galaxy Zoo (Wong et al. 2025), whose number counts have been downscaled to ease comparison of the overall shape in the distribution. Intriguingly, in Figure 9a, we see an ‘excess’ in the G4Jy Sample (for *W1* magnitudes below ~ 14 mag) that warrants further investigation.

We first see whether this excess has a connection to the radio morphology of the source (Figure 9b). Whilst each of the constituent histograms (for ‘single’, ‘double’, ‘triple’, and ‘complex’ morphologies) show hints of an excess at bright *W1* magnitudes, it remains difficult to interpret why this may be the case. A more-informative approach is to split the sample into spectroscopic-redshift bins (Figure 9c), as doing so shows an interesting correspondence for the $0.0 < z_{\text{sp}} < 0.5$ bin. In fact, as illustrated in Figure 9d, the *W1*-magnitude distribution for sources at $0.0 < z_{\text{sp}} < 0.5$ can be modelled by two Gaussian distribution functions: one with a mean of $\mu_1 = 12.1$, corresponding to the ‘excess’, and the other with a mean of $\mu_1 = 15.3$, corresponding to the majority of the *W1* distribution.

Next we consider what could be contributing towards the brighter-magnitude Gaussian ($\mu_1 = 12.1$) that describes the observed excess. The brighter magnitudes could be the result of these sources being part of merging systems or are in particularly-dense environments such as clusters. We can test the latter by cross-matching the G4Jy Sample with the optical-based cluster catalogue produced by Wen & Han (2024), using a match radius of 1 arcsec. This results in 163 cross-matched G4Jy sources (red, unfilled histogram in Figure 9e), 106 of which are at $0.0 < z_{\text{cluster}} < 0.5$ (orange, filled histogram in Figure 9e). Judging by the distribution of the latter, we have good reason to believe that the excess in bright *W1* magnitudes is the result of low-redshift ($z < 0.5$) G4Jy sources being harboured by clusters. The reason that this may not be seen in the *W1* distribution for FIRST galaxies in Radio Galaxy Zoo is that the FIRST survey (Becker et al. 1995; White et al. 1997) is not as sensitive towards diffuse emission as GLEAM, and so the hosts of diffuse radio-galaxies (like those found in cluster environments) do not feature.

4.2.3 *Infrared-faint radio-sources*

Now we briefly consider how the *W1* magnitude can provide an indication of how distant the host galaxy is, noting that mid-infrared

faintness has shown to be an effective criterion for identifying high-redshift radio galaxies (e.g. Norris et al. 2006; Orenstein et al. 2019). In Figure 10 we present the median spectroscopic redshift as a function of *W1* magnitude, where we have only considered magnitude bins that contain a minimum of five spectroscopically-confirmed G4Jy sources. As expected, the median redshift shows an upwards trend as the *W1* magnitude gets fainter, with the $z = 1$ threshold being crossed at ~ 15.25 mag. We note that 20 per cent of the 3CRR sample (i.e. 35 sources) are at $z > 1$, whilst the same can be said for 5 per cent of the G4Jy Sample (i.e. 84 sources), bearing in mind that the latter (currently) has a spectroscopic completeness of 34 per cent (White et al. 2026). It is also worthwhile noting that the highest redshift in the sample – acquired via NED, $z_{\text{NED}} = 3.5699$ (van Ojik et al. 1996) – is for G4Jy 1020, with *W1* = 17.638 mag. Only eight other sources have a fainter *W1* magnitude, and one of these is G4Jy 1456 (aka 4C 13.66) at $z_{\text{NED}} = 1.45$, which was the last 3CRR source to be spectroscopically confirmed (Rawlings et al. 1996).

4.3 Near-infrared properties

The *K*-band traces old stellar populations in galaxies, with the *K*-band luminosity shown by Kauffmann & Charlot (1998) to be a good measure of the underlying stellar mass of the system. This holds out to high redshift, except in the case of quasars, where the near-infrared continuum is dominated by the accretion disc rather than host-galaxy light. As such, the *K*-*z* relation can be used as a diagnostic for distinguishing quasars from the general galaxy population.

In Figure 11 we plot *K*-*z* datapoints for the G4Jy Sample, firstly as a function of the origin of the redshift measurement (Figure 11a). This is mainly for interest, as we do not expect to see any particular trends with respect to the different redshift origins. Despite 6dFGS (Jones et al. 2009) being a relatively-shallow optical survey, its datapoints span a large area of the parameter space, up to $z \sim 1$, and (relevant for the *y*-axis) we remind the reader that the $10\text{-}\sigma$ depth of the *K_S*-band data from 2MASS is 14.3 mag (Section 2.3). Also plotted (in all three panels of Figure 11) is the empirical relation found by Willott et al. (2003) for radio galaxies in the 7C Redshift Survey (Willott et al. 1998) and other Cambridge-based surveys (e.g. 3CRR). This was derived by fitting *K*-band magnitudes obtained through a 64-kpc aperture (so taking the redshift of the source into account). Interestingly, they found a remarkable correspondence in this fitted *K*-*z* relation with the “apparent *K*-magnitude evolution of a galaxy of local luminosity $3L_*$ [that] forms all of its stars in an instantaneous burst at $z_f = 10$ ”. We plan to follow up on this when we have star-formation histories for the G4Jy Sample.

Next, in Figure 11b, we plot *K*-*z* parameter space as a function of spectral curvature, SCI_0 (Equation 1), for G4Jy-NVSS sources. This is in order to see whether there is any correspondence between the (radio) spectral behaviour of the source and its *K_S* magnitude (a proxy for stellar mass) or redshift. As we saw in Figure 8b, there appears to be no correspondence, again suggesting a disconnect between the AGN lifecycle and the host galaxy. **This points towards an external factor that governs the AGN lifecycle, such as the frequency with which gas may lose sufficient angular momentum in order to accrete onto the supermassive black-hole.** The magnetic field within the environment may also play an important role, as discussed for Figure 6b.

Lastly, in Figure 11c we present *K*-*z* space as a function of optical morphology (as classified for the Legacy Surveys DR10; Dey et al. 2019). As expected, there is a predominance of sources with PSF-fitted light-profiles (i.e., quasars) to the right of the *K*-*z* relation determined by Willott et al. (2003). (For reference, 20 per cent of the

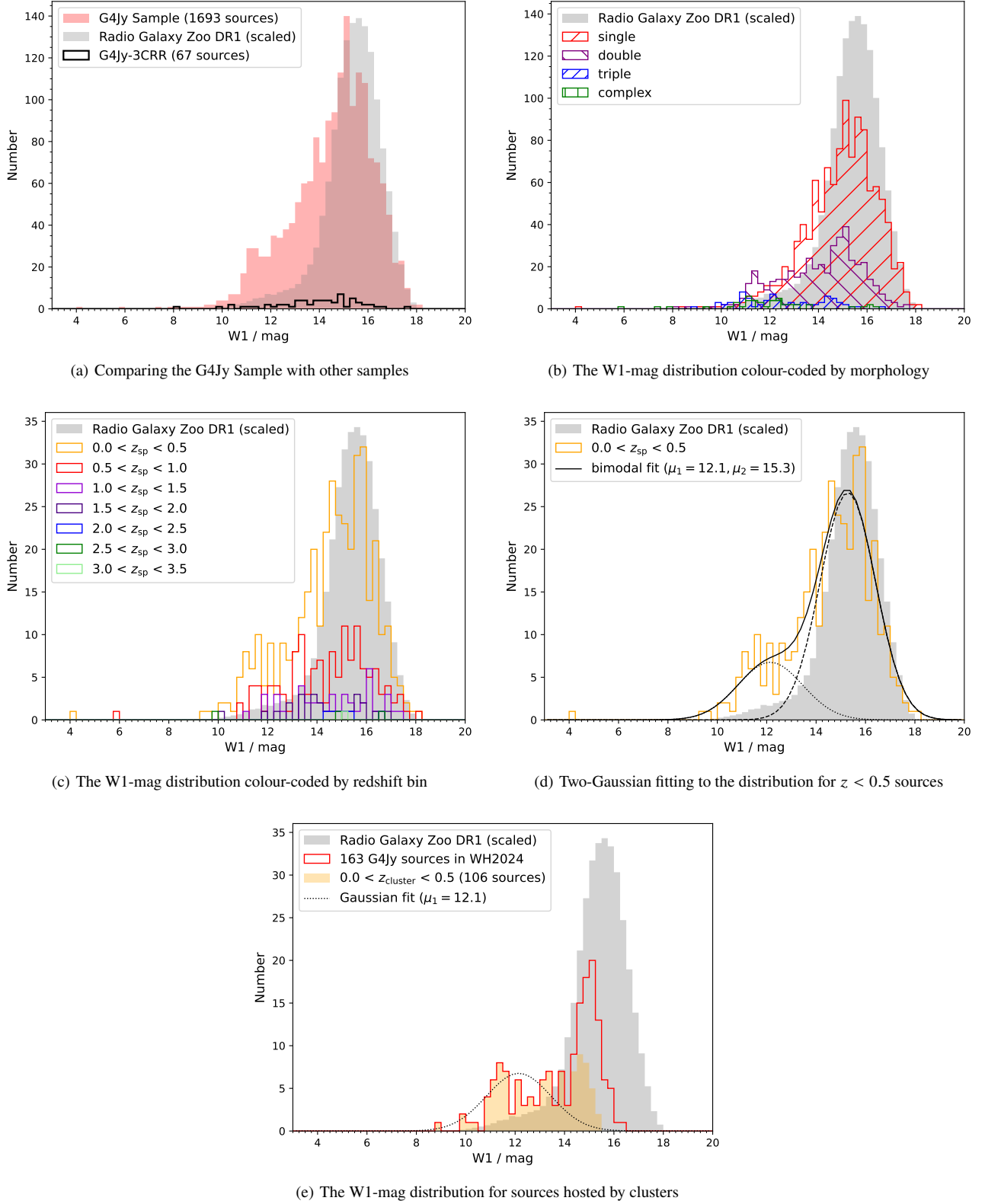


Figure 9. AllWISE-W1 magnitude distributions for the G4Jy Sample (Section 4.2.2). Spectroscopic redshifts are used for panels (c) to (d), to help investigate the origin of the ‘excess’ of brighter W1 magnitudes seen below W1~14 mag, with respect to the Radio Galaxy Zoo DR1 (Wong et al. 2025) FIRST-based (Becker et al. 1995; White et al. 1997) catalogue. The two Gaussians that are fitted in panel (d) have mean and standard deviations of $\mu_1 = 12.1$, $\mu_2 = 15.3$ and $\sigma_1 = 1.31$, $\sigma_2 = 1.12$, respectively. Just the first of these Gaussians is retained for panel (e), for clarity, whilst ‘WH2024’ refers to the cluster catalogue of Wen & Han (2024).

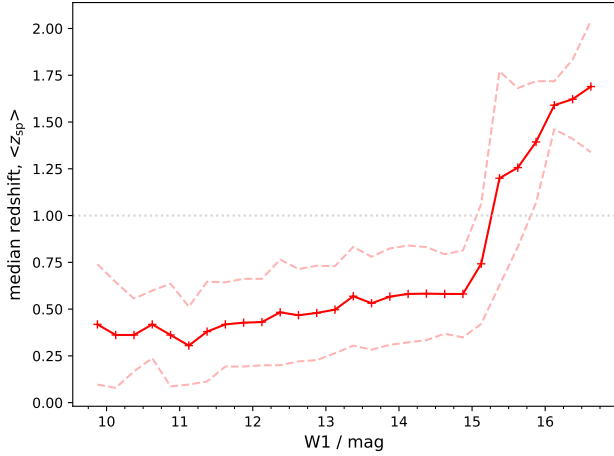


Figure 10. The red, solid line represents the median spectroscopic redshift per bin in AllWISE-W1 magnitude (Figure 9), while the pale-red, dashed lines signify its median absolute deviation. This figure indicates that we can expect to find high redshifts ($z > 1$) for sources that are fainter than W1 ~ 15.25 mag (Vega), as expanded upon in Section 4.2.3.

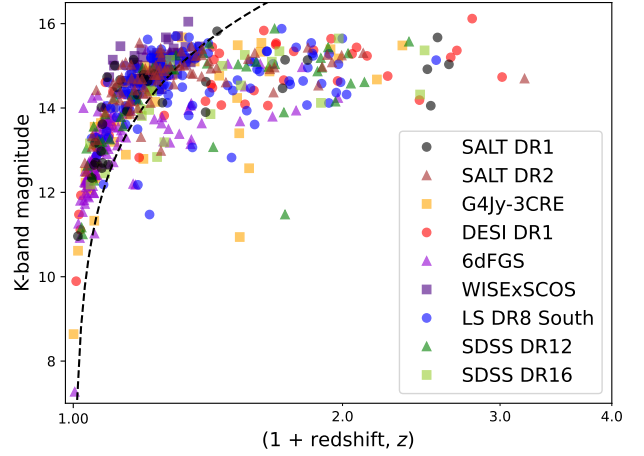
G4Jy Sample has a host galaxy described by a ‘PSF’ light-profile.) A few sources of other optical morphology can also be found to the right of the dashed line, and we suggest that these are starbursts. This is because the connection between stellar mass and the apparent K -band magnitude no longer holds for extreme starbursting systems (e.g. Kauffmann & Charlot 1998), with the additional possibility that the starburst is combined with a quasar as part of a gas-rich merger (e.g. Hopkins et al. 2008). Furthermore, we confirm that there are no sources with exponential-fitted light-profiles (‘EXP’; i.e., spiral galaxies) that have K -band magnitudes. This may be because their stellar masses are too low for them to be detected in 2MASS, and/or they are extremely dust-obscured (da Cunha et al. 2010; Triani et al. 2021).

5 CONCLUSIONS

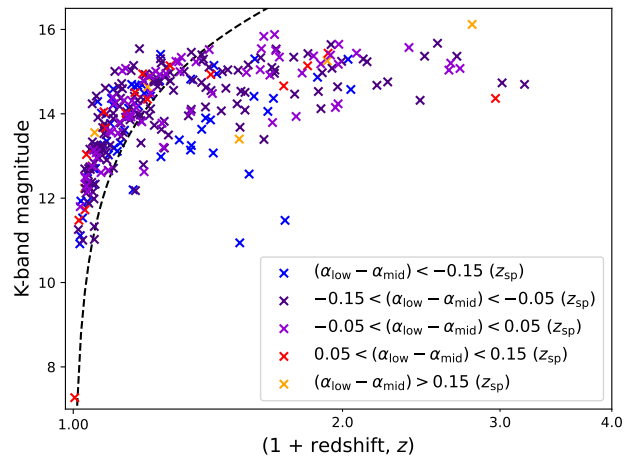
The previous paper in the series, Paper III, detailed the additional work that has gone into host-galaxy identification for the G4Jy Sample, alongside careful assessment of the various redshifts that are available in the literature. The resulting catalogue, which is further updated during the current work, Paper IV (Section 3), forms the basis of our in-depth multiwavelength analysis of G4Jy sources, where we consider their radio, mid-infrared and near-infrared properties (Section 4). A unique feature of this analysis is the incorporation of radio-spectral-curvature information, and we summarise our conclusions as follows:

(i) Crossmatching the G4Jy Sample with DR10 of the (DESI) Legacy Surveys (LS; Dey et al. 2019) results in $griz$ photometry for 1,299 sources. These surveys also provide optical morphology in the form of light-profile fitting by THE TRACTOR (Lang et al. 2016). This information, in addition to basic ancillary data from the NASA/IPAC Extragalactic Database, is provided in the multiwavelength G4Jy catalogue (Section 3, Appendix A).

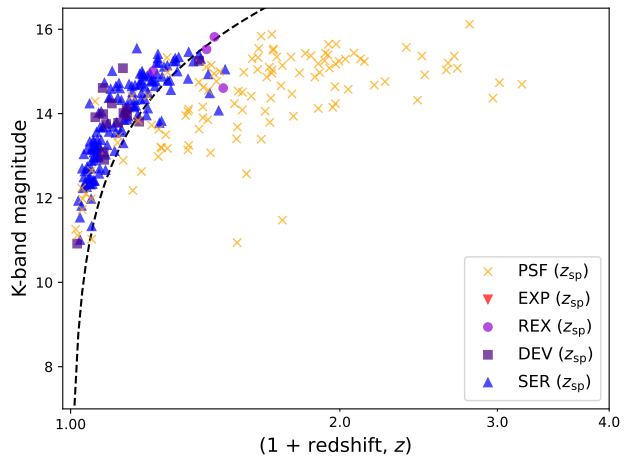
(ii) We leverage the excellent spectral coverage provided by the MWA (over 72–231 MHz) to study the degree of (radio) spectral curvature across the sample. This is simplified through the comparison of spectral indices (α , following $S_\nu \propto \nu^\alpha$), where the spectral



(a) K - z space, by redshift origin



(b) K - z space, by spectral curvature



(c) K - z space, by optical morphology

Figure 11. The K - z datapoints for the G4Jy Sample (Section 4.3), colour-coded by (a) the origin of the spectroscopic/photometric redshift, (b) the degree of spectral curvature in the radio (Equation 1), and (c) the optical morphology (Table 1). A reminder that ‘WISExSCOS’ and ‘LS DR8 South’ are photometric-redshift catalogues, and so they do not have markers that appear in panels (b) and (c), which involve purely spectroscopic redshifts (z_{sp}). In each panel, the dashed line represents the empirical relation found by Willott et al. (2003) through K -band imaging for radio galaxies in the 7C Redshift Survey (7CRS; Willott et al. 1998) and other samples (incl. 3CRR).

curvature index (SCI_0) is defined as $\alpha_{\text{low}} - \alpha_{\text{mid}}$. (For our study, $\alpha_{\text{low}} = \alpha_{72\text{MHz}}^{231\text{MHz}}$ and $\alpha_{\text{mid}} = \alpha_{151\text{MHz}}^{1400\text{MHz}}$.) After dividing the G4Jy Sample into five spectral-curvature bins, we propose that sources with $SCI_0 < -0.15$ are candidate restarted radio-galaxies, whilst sources with $SCI_0 > 0.15$ are candidate remnant radio-galaxies. (This will be tested through visual inspection of deeper, higher-resolution radio-images than those currently available, in addition to modelling the age of the radio emission.) We note that observational bias may explain the tendency for *spectroscopically-confirmed* candidate remnant radio-galaxies to be found at lower redshift than the rest of the radio-galaxy population. Moreover, spectral flattening at low frequencies (due to absorption effects) complicates the interpretation of the SCI parameter as a proxy for spectral age. This will be explored in future work.

(iii) No trend is seen in spectral curvature whether the 151-MHz radio-luminosities or the 1400-MHz radio-luminosities are presented. We also present the linear sizes as a function of spectral curvature, but no trends are evident either.

(iv) Following the 1-Mpc threshold of Willis & Strom (1978), we list 11 GRGs in Table C1, noting that the angular sizes provided there are larger than those in the G4Jy catalogue, which need to be refined.

(v) **The radio-power–size (P – D) diagram (Baldwin 1982) is an informative way of studying the evolutionary paths of radio galaxies**, where sources move from the left-hand side to the right-hand side of the diagram as they expand and fade during their lifetime (see also Ryle & Longair 1967). Following on from White et al. (2025), we present the P – D diagram as a function of radio morphology, and note the distinctive distribution of ‘single’ sources (Figure 5). Those that belong to a trunk-like region in P – D space likely have radio-jets that are significantly slowed by the surrounding medium (and so are ‘frustrated’ radio-sources), or are simply *young* radio-sources. Meanwhile, the ‘single’ sources that span a range of linear sizes beyond this ‘trunk’ are interpreted as FR-I or FR-II radio-galaxies that cannot be spatially resolved in NVSS imaging. Also, as expected, the ‘doubles’ and ‘triples’ extend to larger linear sizes for a range of radio luminosities (see also the distribution of FR-II radio-galaxies in figure 6 by Chilufya et al. 2025).

(vi) **For the first time, we combine the radio luminosity and the linear size with the degree of spectral curvature, i.e. [P – D](SCI_0), which approximates the spectral age of the source (Figure 6b)** – although, see the caveat above [item (ii)]. This leads to two intriguing observations: (a) that there is a predominance of candidate remnant radio-galaxies at $D < 200$ kpc (suggesting that the radio-jets are growing slowly on the same spatial scales as the circumgalactic medium), and (b) that candidate restarted radio-galaxies extend to GRG sizes (suggesting that the supermassive black-hole has been reignited following a long ‘duty cycle’ of the AGN). However, the former interpretation is complicated by the presence of young radio-sources, which exhibit similar SCI_0 values as remnant radio-galaxies.

(vii) As previously shown by Gürkan et al. (2014); Jarrett et al. (2017), and other authors, radio galaxies populate the entirety of *WISE* colour-colour space. We see no trend with respect to either the radio morphology or the spectral curvature of the G4Jy source, but there is correspondence between the sources whose (optical) light-profile is PSF-fitted and the ‘quasar’ region of this colour-colour space.

(viii) Investigation of the $W1$ -magnitude distribution appears to confirm that the ‘excess’ of bright magnitudes (with respect to the distribution for Radio Galaxy Zoo; Wong et al. 2025) could be explained by low-redshift ($z < 0.5$) G4Jy sources that have diffuse radio-emission and are harboured by clusters. In addition, we find that the median spectroscopic-redshift crosses the $z = 1$ threshold at

$W1 \sim 15.25$ mag, which demonstrates the effectiveness of using mid-infrared faintness to identify candidate high-redshift radio-galaxies.

(ix) The K -band magnitude is a good proxy for the stellar mass of the host galaxy, with the well-studied K – z relation (Willott et al. 2003) allowing for quasars to be distinguished from the rest of the galaxy population. We see that this is the case for G4Jy sources when the optical morphology (‘PSF’) is considered as a quasar classification. No trends are seen when datapoints are plotted in K – z space as a function of redshift origin or spectral curvature of the radio emission.

(x) To repeat: **no trends are seen with respect to spectral curvature and the location of the source in either *WISE* colour-colour space or K – z space. This suggests an expected disconnect between spectral-curvature properties and the host galaxy, which points towards an external factor that influences the radio lifecycle of the source.** Given the recurrent activity that we witness for restarted radio-galaxies, this could be the frequency with which gas accretes onto the central supermassive black-hole.

As shown, *multiwavelength* data analysis is crucial for investigating the physical processes that govern how galaxies evolve. The *legacy multiwavelength dataset* that we have compiled in this work (Papers III and IV; White et al., 2025c, 2025d) will therefore enable detailed analysis of the G4Jy Sample, and we expect this to be supplemented by many more datasets, such as X-ray information.

ACKNOWLEDGEMENTS

We thank the referee for their comments, which helped to improve the manuscript. In addition, we thank Dustin Lang and Ross Turner for helpful discussions, and those involved in the Astro Data Lab Science Platform (<https://datalab.noirlab.edu/>).

This work is based on the research supported in part by the National Research Foundation of South Africa (Grant Number 151060). The financial assistance of the South African Radio Astronomy Observatory (SARAO) towards this research is also hereby acknowledged. CJR acknowledges support from the DFG via the Collaborative Research Center SFB1491, *Cosmic Interacting Matters – From Source to Signal* (project no. 445052434).

Some of the observations reported in this paper were obtained with the Southern African Large Telescope (SALT), under program 2020-1-MLT-008 (PI: White). Additional data were obtained via the MeerKAT telescope (via proposal SCI-20190418-SW-01). This is operated by SARAO, which is a facility of the National Research Foundation, an agency of the Department of Science and Innovation.

This research uses services or data provided by the Astro Data Lab, which is part of the Community Science and Data Center (CSDC) Program of NSF NOIRLab. NOIRLab is operated by the Association of Universities for Research in Astronomy (AURA), Inc. under a cooperative agreement with the U.S. National Science Foundation.

This research has made use of the NASA/IPAC Extragalactic Database (NED), which is funded by the National Aeronautics and Space Administration and operated by the California Institute of Technology.

The National Radio Astronomy Observatory is a facility of the National Science Foundation operated under cooperative agreement by Associated Universities, Inc.

This publication makes use of data products from the Two Micron All Sky Survey, which is a joint project of the University of Massachusetts and the Infrared Processing and Analysis Center/California Institute of Technology, funded by the National Aero-

navitics and Space Administration and the National Science Foundation.

This scientific work uses data obtained from Inyarrimanha Ilgari Bundara / the Murchison Radio-astronomy Observatory. We acknowledge the Wajarri Yamaji People as the Traditional Owners and native title holders of the Observatory site. CSIRO's ASKAP radio telescope is part of the Australia Telescope National Facility (<https://ror.org/05qajvd42>). Operation of ASKAP is funded by the Australian Government with support from the National Collaborative Research Infrastructure Strategy. ASKAP uses the resources of the Pawsey Supercomputing Research Centre. Establishment of ASKAP, Inyarrimanha Ilgari Bundara, the CSIRO Murchison Radio-astronomy Observatory and the Pawsey Supercomputing Research Centre are initiatives of the Australian Government, with support from the Government of Western Australia and the Science and Industry Endowment Fund. This paper includes archived data obtained through the CSIRO ASKAP Science Data Archive, CASDA (<https://data.csiro.au>).

Funding for the Sloan Digital Sky Survey IV has been provided by the Alfred P. Sloan Foundation, the U.S. Department of Energy Office of Science, and the Participating Institutions. SDSS-IV acknowledges support and resources from the Center for High Performance Computing at the University of Utah. The SDSS website is www.sdss.org. SDSS-IV is managed by the Astrophysical Research Consortium for the Participating Institutions of the SDSS Collaboration including the Brazilian Participation Group, the Carnegie Institution for Science, Carnegie Mellon University, Center for Astrophysics | Harvard & Smithsonian, the Chilean Participation Group, the French Participation Group, Instituto de Astrofísica de Canarias, The Johns Hopkins University, Kavli Institute for the Physics and Mathematics of the Universe (IPMU) / University of Tokyo, the Korean Participation Group, Lawrence Berkeley National Laboratory, Leibniz Institut für Astrophysik Potsdam (AIP), Max-Planck-Institut für Astronomie (MPIA Heidelberg), Max-Planck-Institut für Astrophysik (MPA Garching), Max-Planck-Institut für Extraterrestrische Physik (MPE), National Astronomical Observatories of China, New Mexico State University, New York University, University of Notre Dame, Observatório Nacional / MCTI, The Ohio State University, Pennsylvania State University, Shanghai Astronomical Observatory, United Kingdom Participation Group, Universidad Nacional Autónoma de México, University of Arizona, University of Colorado Boulder, University of Oxford, University of Portsmouth, University of Utah, University of Virginia, University of Washington, University of Wisconsin, Vanderbilt University, and Yale University.

DATA AVAILABILITY

The updated G4Jy catalogue will be made available through VizieR (Ochsenbein et al. 2000) and the GitHub repository for the G4Jy Sample: <https://github.com/svw26/G4Jy>. Overlays for the full sample, amongst other G4Jy data, can be downloaded from the Zenodo repository: <https://zenodo.org/communities/g4jy/>. We encourage others to also make their G4Jy data available here, in the interest of Open Access, discoverability, and general best practices (Chen et al. 2022).

REFERENCES

- Abazajian K. N., et al., 2009, *ApJS*, **182**, 543
 Alexander P., Leahy J. P., 1987, *MNRAS*, **225**, 1
 An T., Baan W. A., 2012, *ApJ*, **760**, 77
 Andernach H., Brügger M., 2025, *A&A*, **699**, A257
 Andernach H., Jiménez-Andrade E. F., Willis A. G., 2021, *Galaxies*, **9**, 99
 Antonucci R., 1993, *ARA&A*, **31**, 473
 Baldwin J. E., 1982, in Heeschen D. S., Wade C. M., eds, IAU Symposium Vol. 97, Extragalactic Radio Sources. pp 21–24
 Barthel P. D., 1989, *ApJ*, **336**, 606
 Becker R. H., White R. L., Helfand D. J., 1995, *ApJ*, **450**, 559
 Bertin E., 2011, in Evans I. N., Accomazzi A., Mink D. J., Rots A. H., eds, Astronomical Society of the Pacific Conference Series Vol. 442, Astronomical Data Analysis Software and Systems XX. p. 435
 Bertin E., Arnouts S., 1996, *A&AS*, **117**, 393
 Best P. N., Heckman T. M., 2012, *MNRAS*, **421**, 1569
 Bhatnagar S., Gopal-Krishna Wisotzki L., 1998, *MNRAS*, **299**, L25
 Bilicki M., et al., 2016, *ApJS*, **225**, 5
 Blumenthal G., Miley G., 1979, *A&A*, **80**, 13
 Callingham J. R., et al., 2017, *ApJ*, **836**, 174
 Chen T. X., et al., 2022, *ApJS*, **260**, 5
 Chilufya J., Hardcastle M. J., Pierce J. C. S., Drake A. B., Baldi R. D., Röttgering H. J. A., Smith D. J. B., 2025, *MNRAS*, **539**, 463
 Collier J. D., et al., 2014, *MNRAS*, **439**, 545
 Condon J. J., 1992, *ARA&A*, **30**, 575
 Condon J. J., Cotton W. D., Greisen E. W., Yin Q. F., Perley R. A., Taylor G. B., Broderick J. J., 1998, *AJ*, **115**, 1693
 Condon J. J., Cotton W. D., White S. V., Legodi S., Goedhart S., McAlpine K., Ratcliffe S. M., Camilo F., 2021, *ApJ*, **917**, 18
 Croton D. J., et al., 2006, *MNRAS*, **365**, 11
 Cutri R. M., et al., 2003, 2MASS All Sky Catalog of point sources.
 Cutri R. M., et al., 2013, Explanatory Supplement to the AllWISE Data Release Products, Explanatory Supplement to the AllWISE Data Release Products, by R. M. Cutri et al.
 DESI Collaboration et al., 2025, *arXiv e-prints*, p. [arXiv:2503.14745](https://arxiv.org/abs/2503.14745)
 Dabhade P., et al., 2020, *A&A*, **635**, A5
 Davies J. J., Crain R. A., Oppenheimer B. D., Schaye J., 2020, *MNRAS*, **491**, 4462
 De Breuck C., van Breugel W., Röttgering H. J. A., Miley G., 2000, *A&AS*, **143**, 303
 Dey A., et al., 2019, *AJ*, **157**, 168
 Do T., et al., 2019, *Science*, **365**, 664
 Duncan K. J., 2022, *MNRAS*, **512**, 3662
 Dunne L., Eales S. A., 2001, *MNRAS*, **327**, 697
 Dunne L., Eales S., Edmunds M., Ivison R., Alexander P., Clements D. L., 2000, *MNRAS*, **315**, 115
 Event Horizon Telescope Collaboration et al., 2019, *ApJ*, **875**, L1
 Flaugher B., et al., 2015, *AJ*, **150**, 150
 Franzen T. M. O., et al., 2021, *Publ. Astron. Soc. Australia*, **38**, e041
 Gaia Collaboration et al., 2018, *A&A*, **616**, A1
 García-Pérez A., et al., 2024, *ApJS*, **271**, 8
 Godfrey L. E. H., Morganti R., Brienza M., 2017, *MNRAS*, **471**, 891
 Gopal-Krishna 1988, *A&A*, **192**, 37
 Gordon Y. A., et al., 2020, *Research Notes of the American Astronomical Society*, **4**, 175
 Gürkan G., Hardcastle M. J., Jarvis M. J., 2014, *MNRAS*, **438**, 1149
 Hardcastle M. J., 2018, *MNRAS*, **475**, 2768
 Hardcastle M. J., Croston J. H., 2020, *New Astron. Rev.*, **88**, 101539
 Hardcastle M. J., Krause M. G. H., 2013, *MNRAS*, **430**, 174
 Hardcastle M. J., Krause M. G. H., 2014, *MNRAS*, **443**, 1482
 Hardcastle M. J., et al., 2019, *A&A*, **622**, A12
 Harwood J. J., Hardcastle M. J., Croston J. H., Goodger J. L., 2013, *MNRAS*, **435**, 3353
 Hopkins P. F., Hernquist L., Cox T. J., Kereš D., 2008, *ApJS*, **175**, 356
 Hurley-Walker N., et al., 2017, *MNRAS*, **464**, 1146
 Ineson J., Croston J. H., Hardcastle M. J., Mingo B., 2017, *MNRAS*, **467**, 1586
 Ishibashi W., Fabian A. C., 2012, *MNRAS*, **427**, 2998
 Jaffe W. J., Perola G. C., 1973, *A&A*, **26**, 423
 Jamrozny M., Klein U., Mack K. H., Gregorini L., Parma P., 2004, *A&A*, **427**, 79

- Jarrett T. H., Chester T., Cutri R., Schneider S., Skrutskie M., Huchra J. P., 2000, *AJ*, **119**, 2498
- Jarrett T. H., et al., 2017, *ApJ*, **836**, 182
- Jones P. A., McAdam W. B., 1992, *ApJS*, **80**, 137
- Jones D. H., et al., 2009, *MNRAS*, **399**, 683
- Kardashev N. S., 1962, *Soviet Ast.*, **6**, 317
- Kauffmann G., Charlot S., 1998, *MNRAS*, **297**, L23
- Lacy M., et al., 2020, *PASP*, **132**, 035001
- Laing R. A., Peacock J. A., 1980, *MNRAS*, **190**, 903
- Laing R. A., Riley J. M., Longair M. S., 1983, *MNRAS*, **204**, 151
- Lammers C., Iyer K. G., Ibarra-Medel H., Pacifici C., Sánchez S. F., Tacchella S., Woo J., 2023, *ApJ*, **953**, 26
- Lang D., Hogg D. W., Mykytyn D., 2016, The Tractor: Probabilistic astronomical source detection and measurement
- Lawrence A., Elvis M., 1982, *ApJ*, **256**, 410
- Lindgren L., et al., 1994, in Breckinridge J. B., ed., Society of Photo-Optical Instrumentation Engineers (SPIE) Conference Series Vol. 2200, Amplitude and Intensity Spatial Interferometry II. pp 599–608, doi:10.1117/12.177278
- Lister M. L., 2003, *ApJ*, **599**, 105
- Machalski J., Koziel-Wierzbowska D., Jamroz M., 2007, *Acta Astron.*, **57**, 227
- Madau P., Dickinson M., 2014, *ARA&A*, **52**, 415
- Mahatma V. H., et al., 2018, *MNRAS*, **475**, 4557
- Malarecki J. M., Staveley-Smith L., Saripalli L., Subrahmanyan R., Jones D. H., Duffy A. R., Rioja M., 2013, *MNRAS*, **432**, 200
- Mauch T., Sadler E. M., 2007, *MNRAS*, **375**, 931
- Mauch T., Murphy T., Buttery H. J., Curran J., Hunstead R. W., Piestrzynski B., Robertson J. G., Sadler E. M., 2003, *MNRAS*, **342**, 1117
- McAlpine K., et al., 2015, in Advancing Astrophysics with the Square Kilometre Array (AASKA14). p. 83 (arXiv:1412.5771), doi:10.22323/1.215.0083
- McConnell D., et al., 2020, *Publ. Astron. Soc. Australia*, **37**, e048
- McMahon R. G., Banerji M., Gonzalez E., Kuposov S. E., Bejar V. J., Lodiou N., Rebolo R., VHS Collaboration 2021, VizieR Online Data Catalog: The VISTA Hemisphere Survey (VHS) catalog DR5 (McMahon+, 2020), VizieR On-line Data Catalog: II/367. Originally published in: 2013Msngr.154...35M
- Miley G., 1980, *ARA&A*, **18**, 165
- Mullin L. M., Riley J. M., Hardcastle M. J., 2008, *MNRAS*, **390**, 595
- Murgia M., et al., 2011, *A&A*, **526**, A148
- Murphy T., Mauch T., Green A., Hunstead R. W., Piestrzynska B., Kels A. P., Sztajer P., 2007, *MNRAS*, **382**, 382
- Norris R. P., et al., 2006, *AJ*, **132**, 2409
- Ochsenbein F., Bauer P., Marcout J., 2000, *A&AS*, **143**, 23
- Onuora L. I., 1989, *Ap&SS*, **162**, 349
- Orenstein B. J., Collier J. D., Norris R. P., 2019, *MNRAS*, **484**, 1021
- Owen F. N., Ledlow M. J., Keel W. C., 1995, *AJ*, **109**, 14
- Pacholczyk A. G., 1970, Radio astrophysics. Nonthermal processes in galactic and extragalactic sources
- Pier E. A., Krolik J. H., 1992, *ApJ*, **401**, 99
- Pinjarkar S., et al., 2025, *MNRAS*, **537**, 3481
- Pogge R. W., 1988, *ApJ*, **328**, 519
- Proctor D. D., 2016, *ApJS*, **224**, 18
- Quici B., et al., 2021, *Publ. Astron. Soc. Australia*, **38**, e008
- Quici B., Turner R. J., Seymour N., Hurley-Walker N., 2025, *MNRAS*, **537**, 343
- Rawlings S., Lacy M., Leahy J. P., Dunlop J. S., Garrington S. T., Ludke E., 1996, *MNRAS*, **279**, L13
- Rees M. J., 1966, *Nature*, **211**, 468
- Richstone D., et al., 1998, *Nature*, **385**, A14
- Rocca-Volmerange B., Guiderdoni B., 1990, *MNRAS*, **247**, 166
- Roettgering H. J. A., Lacy M., Miley G. K., Chambers K. C., Saunders R., 1994, *A&AS*, **108**, 79
- Ryle Sir M., Longair M. S., 1967, *MNRAS*, **136**, 123
- Sabater J., et al., 2019, *A&A*, **622**, A17
- Sanders D. B., Phinney E. S., Neugebauer G., Soifer B. T., Matthews K., 1989, *ApJ*, **347**, 29
- Saripalli L., Gopal-Krishna Reich W., Kuehr H., 1986, *A&A*, **170**, 20
- Saripalli L., Hunstead R. W., Subrahmanyan R., Boyce E., 2005, *AJ*, **130**, 896
- Saxena A., et al., 2018, *MNRAS*, **480**, 2733
- Schoenmakers A. P., de Bruyn A. G., Röttgering H. J. A., van der Laan H., Kaiser C. R., 2000, *MNRAS*, **315**, 371
- Sejake P. K., White S. V., Heywood I., Thorat K., Bester H. L., Makhathini S., Fanaroff B., 2023, *MNRAS*, **518**, 4290
- Sérsic J. L., 1963, Boletín de la Asociacion Argentina de Astronomia La Plata Argentina, **6**, 41
- Shabala S. S., Jurlin N., Morganti R., Brienza M., Hardcastle M. J., Godfrey L. E. H., Krause M. G. H., Turner R. J., 2020, *MNRAS*, **496**, 1706
- Shimwell T. W., et al., 2019, *A&A*, **622**, A1
- Shimwell T. W., et al., 2022, *A&A*, **659**, A1
- Silk J., 2013, *ApJ*, **772**, 112
- Silva D. R., et al., 2016, in American Astronomical Society Meeting Abstracts #228. p. 317.02
- Singh V., et al., 2014, *A&A*, **569**, A52
- Skrutskie M. F., et al., 2006, *AJ*, **131**, 1163
- Smith D. J. B., et al., 2012, *MNRAS*, **427**, 703
- Stern D., et al., 2012, *ApJ*, **753**, 30
- Stewart G. S. C., Shabala S. S., Turner R. J., Yates-Jones P. M., Krause M. G. H., Wong O. I., Power C., Hardcastle M. J., 2025, *arXiv e-prints*, p. arXiv:2511.01193
- Subrahmanyan R., Saripalli L., Hunstead R. W., 1996, *MNRAS*, **279**, 257
- Tingay S. J., et al., 2013, *Publ. Astron. Soc. Australia*, **30**, e007
- Toomre A., Toomre J., 1972, *ApJ*, **178**, 623
- Triani D. P., Sinha M., Croton D. J., Dwek E., Pacifici C., 2021, *MNRAS*, **503**, 1005
- Tritton K. P., Schilizzi R. T., 1973, *MNRAS*, **165**, 245
- Turner R. J., 2018, *MNRAS*, **476**, 2522
- Turner R. J., Shabala S. S., 2015, *ApJ*, **806**, 59
- Turner R. J., Shabala S. S., Krause M. G. H., 2018, *MNRAS*, **474**, 3361
- Turner R. J., Yates-Jones P. M., Shabala S. S., Quici B., Stewart G. S. C., 2023, *MNRAS*, **518**, 945
- Urry C. M., Padovani P., 1995, *PASP*, **107**, 803
- Vardoulaki E., et al., 2024, *arXiv e-prints*, p. arXiv:2412.01795
- Wang Y., Kaiser C. R., 2008, *MNRAS*, **388**, 677
- Wayth R. B., et al., 2015, *Publ. Astron. Soc. Australia*, **32**, e025
- Wen Z. L., Han J. L., 2024, *ApJS*, **272**, 39
- White S. V., 2023, *arXiv e-prints*, p. arXiv:2307.09393
- White S. D. M., Frenk C. S., 1991, *ApJ*, **379**, 52
- White R. L., Becker R. H., Helfand D. J., Gregg M. D., 1997, *ApJ*, **475**, 479
- White S. V., Jarvis M. J., Häußler B., Maddox N., 2015, *MNRAS*, **448**, 2665
- White S. V., Jarvis M. J., Kalfountzou E., Hardcastle M. J., Verma A., Cao Orjales J. M., Stevens J., 2017, *MNRAS*, **468**, 217
- White S. V., et al., 2018, *arXiv e-prints*, p. arXiv:1810.01226
- White S. V., et al., 2020a, *Publ. Astron. Soc. Australia*, **37**, e017
- White S. V., et al., 2020b, *Publ. Astron. Soc. Australia*, **37**, e018
- White S. V., et al., 2025, *Publ. Astron. Soc. Australia*, **42**, e085
- White S. V., et al., 2026, *MNRAS*,
- Wilde M. C., et al., 2023, *ApJ*, **948**, 114
- Williams W. L., et al., 2019, *A&A*, **622**, A2
- Willis A. G., Strom R. G., 1978, *A&A*, **62**, 375
- Willott C. J., Rawlings S., Blundell K. M., Lacy M., 1998, *MNRAS*, **300**, 625
- Willott C. J., Rawlings S., Jarvis M. J., Blundell K. M., 2003, *MNRAS*, **339**, 173
- Wong O. I., et al., 2025, *MNRAS*, **536**, 3488
- Wright E. L., et al., 2010, *AJ*, **140**, 1868
- Yates-Jones P. M., Turner R. J., Shabala S. S., Krause M. G. H., 2022, *MNRAS*, **511**, 5225
- York D. G., et al., 2000, *AJ*, **120**, 1579
- Zou H., et al., 2017, *PASP*, **129**, 064101
- da Cunha E., Eminian C., Charlot S., Blaizot J., 2010, *MNRAS*, **403**, 1894
- de Vaucouleurs G., 1948, *Annales d'Astrophysique*, **11**, 247
- van Ojik R., Roettgering H. J. A., Carilli C. L., Miley G. K., Bremer M. N., Macchetto F., 1996, *A&A*, **313**, 25

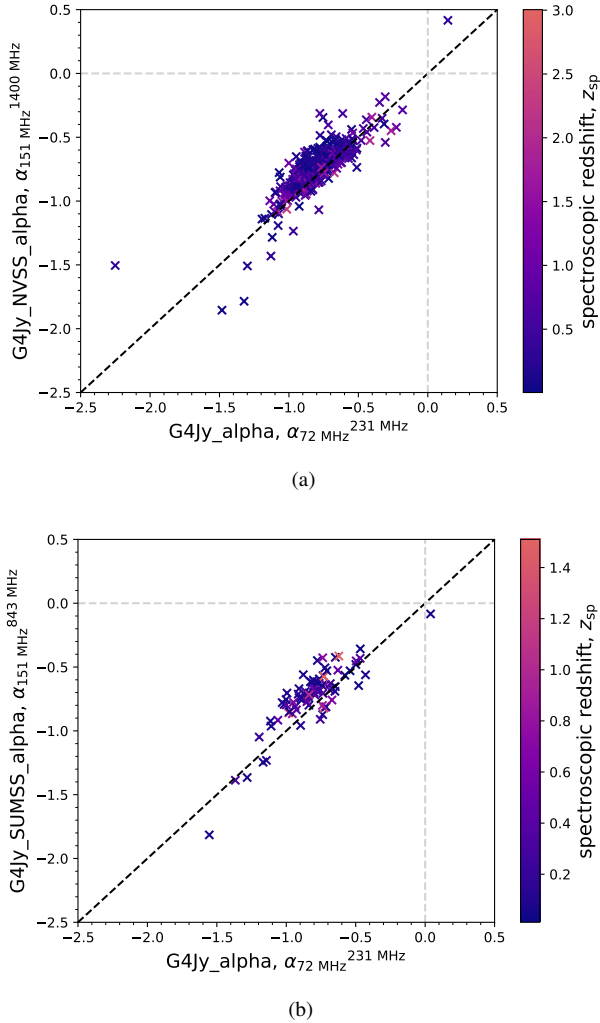


Figure B1. Panels (a) and (b) show different spectral indices from the G4Jy catalogue (White et al. 2020a,b) plotted against each other (Section 4.1.1). Diagonal lines represent the 1:1 relation, which signifies the (narrow) region over which the radio emission between low and ‘mid’ frequencies can accurately be described by a power-law function. The datapoints of each panel are colour-coded by the spectroscopic redshift to help look for any trend with spectral index (Appendix B).

APPENDIX A: COLUMNS (AND AN EXAMPLE ROW) OF THE MULTIWAVELENGTH G4JY CATALOGUE

Descriptions of newly-added/newly-named columns in the multi-wavelength G4Jy catalogue, along with ninth-row entries, can be found in Table A1. Readers who wish to combine the current catalogue with the original G4Jy catalogue (White et al. 2020a,b), in order to retrieve all of the low-frequency radio data (see appendix E of Paper I), are advised to crossmatch the catalogues on the centroid positions (centroid_RAJ2000, centroid_DEJ2000). This is because, unlike the host-galaxy positions, the centroid positions exist for the full sample. In addition, the latter remain fixed, which helps with long-term ‘future-proofing’ of the catalogue.

APPENDIX B: MORE ON SPECTRAL INDICES

Continuing the investigation of spectral curvature detailed in Section 4.1.1, we study the distribution of spectroscopic redshift within the $\alpha_{\text{low}} - \alpha_{\text{mid}}$ plane (Figure B1). We see no tendency for the highest redshifts to be associated with the steepest spectral-indices, which calls into question the efficacy of common methods for identifying high-redshift radio-sources (see also Pinjarkar et al. 2025). However, we note that a much smaller fraction of sources lies below the 1:1 relation than seen in Figure 1. This could be because more-recent AGN activity (relevant for datapoints above the 1:1 relation) correlates with greater photoionisation of the broad- and narrow-line regions, making spectroscopic redshifts easier to obtain. This is in contrast to ageing sources (relevant to the datapoints below the 1:1 relation), which may have little to no AGN-related optical emission.

We also check whether any trends can be seen if the $P-D$ diagram (Section 4.1.4) is plotted as a function of α_{low} or α_{mid} . As shown in Figure B2, and as expected, the distributions appear ‘smooth’ with respect to the spectral index that is used. This is because a single spectral index can take on a wide range values that are all consistent with synchrotron emission. Clearly, spectral curvature is key to exploring the evolutionary states of radio galaxies in further detail (Figure 6b), and we look forward to having more-quantitative results as the G4Jy Sample approaches spectroscopic completeness.

APPENDIX C: GIANT RADIO-GALAXIES

In Table C1 we list the sources that pass the 1-Mpc threshold for categorisation as giant radio-galaxies (GRGs), following the definition by Willis & Strom (1978). Three of these (G4Jy 318, G4Jy 1021, and G4Jy 1079) have new angular-size measurements via VLASS, and we describe another two sources in detail below. In addition, a further three G4Jy sources warrant special discussion in the text. We also note that, as part of creating Table C1, we discard three ‘GRGs’ (G4Jy 155, G4Jy 285, and G4Jy 315) where the linear size is determined via a photometric redshift that is flagged by Duncan (2022) as being ‘unreliable’.

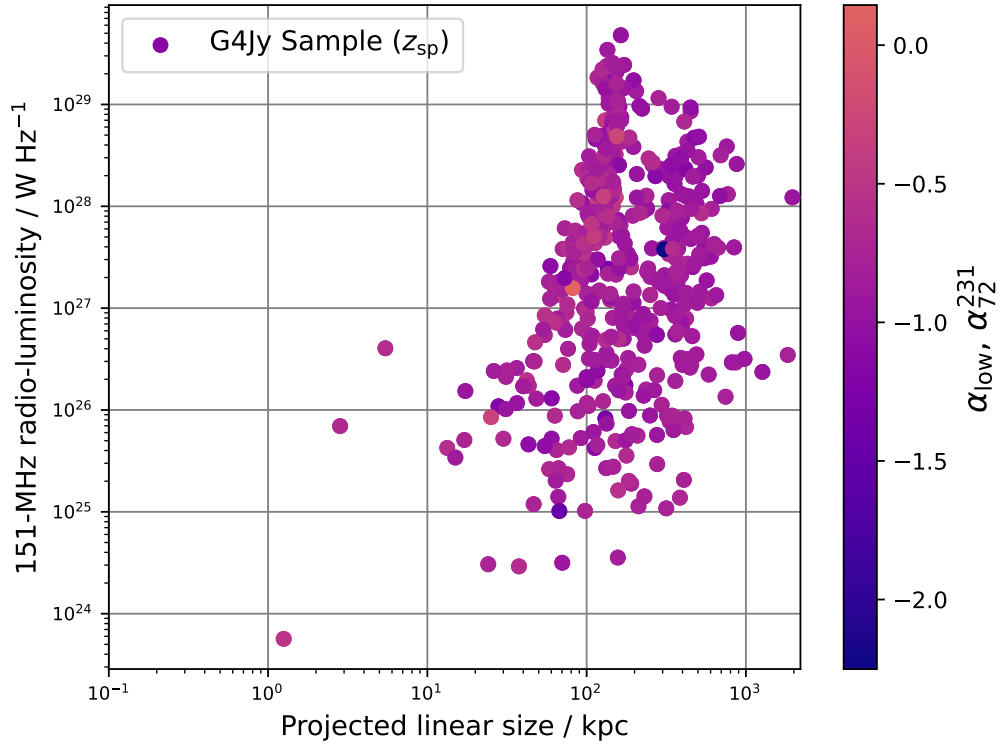
We first turn our attention to **G4Jy 79**, which is quoted as having a linear size of 1078 kpc in the G4Jy catalogue. However, this is based on a photometric redshift of $z_{\text{ph}} = 0.161$, whereas $z_{\text{sp}} = 0.123$ has been measured by Machalski et al. (2007). Combined with an angular size of 5.9 arcmin, as measured in VLASS, the linear size is 780 kpc. Hence, it does not meet our 1-Mpc criterion for a GRG, and so we do not list it in Table C1.

Unfortunately, a photometric redshift in our catalogue leads to another inflated linear size (1165 kpc), this time for **G4Jy 315**. Also known as 3C 75, and previously presented in G4Jy Paper II (White et al. 2020a), this source is associated with a pair of wide-angle-tail radio-galaxies: NGC 1128N and NGC 1128S. They are 16 arcsec apart from each other, and belong to cluster Abell 400 at a redshift of 0.0244 (e.g. Owen et al. 1995). Having measured an angular size of 11.5 arcmin in RACS-low (McConnell et al. 2020), we obtain 340 kpc for its linear size and therefore conclude that G4Jy 315 (NGC 1128N) is not a GRG.

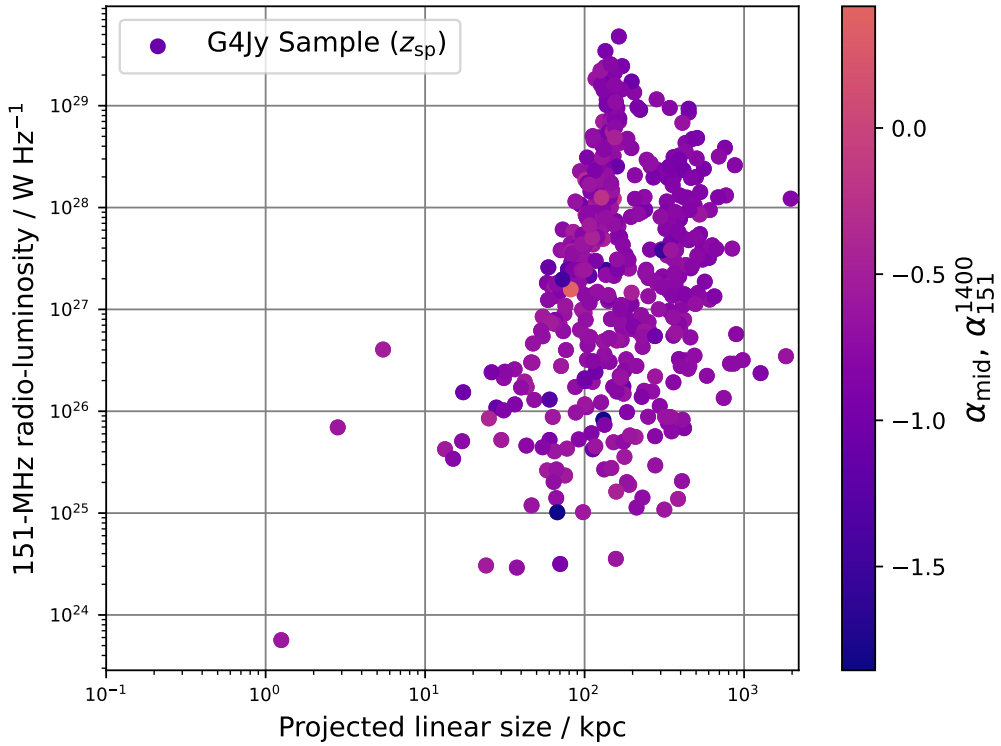
Several groups (Tritton & Schilizzi 1973; Jones & McAdam 1992; Malarecki et al. 2013) have incorrectly proposed WISEA J070530.57–451311.1 as the host galaxy for **G4Jy 641**, whereas the identification of Sejake et al. (2023), WISEA J070532.94–451308.8, is supported by detecting the radio core in a MeerKAT image (see their figure 10). We use this image to measure the angular size (7.77 arcmin) and, in combination with a SALT redshift ($z_{\text{sp}} = 0.128$;

Table A1. Column numbers, names, units, descriptions, and ninth-row entries for 60 of the 131 columns in the updated G4Jy catalogue (Section 3, Appendix A). This row has been chosen to minimise the number of empty columns. Column names with the suffix ‘LSDR10’ indicate that the column data has been obtained from the Legacy Surveys DR10 (Dey et al. 2019). Similarly, ‘wiseScos’ refers to the photometric-redshift catalogue of Bilicki et al. (2016), and ‘LSDR8south’ refers to the photometric-redshift catalogue of Duncan (2022). See appendix E of White et al. (2020b) for the remaining 71 G4Jy-catalogue columns.

Column no.	Column name	Units	Description	Ninth-row entry
2	NED_name	–	Alternative name for the G4Jy source in NED	PKS 0003–56
21	S_1400_Jy	Jy	Total flux-density at 1400 MHz (extrapolated for SUMSS sources)	2.1010
22	err_S_1400_Jy	Jy	Error on the total flux-density at 1400 MHz	0.1413
23	alpha_mid	–	Spectral index, 151 to 1400 MHz (extrapolated for SUMSS sources)	–0.678867
24	err_alpha_mid	–	Error on the spectral index between 151 and 1400 MHz	0.030214
69	host_name	–	Name of the host galaxy	WISEA J000557.94–562831.0
70	host_RAJ2000	deg	Right ascension for the host galaxy (J2000)	1.4914452
71	host_DEJ2000	deg	Declination for the host galaxy (J2000)	–56.475300
80	eeMaj_allwise	arcsec	Semi-major axis of the error ellipse	0.0508
81	eeMin_allwise	arcsec	Semi-minor axis of the error ellipse	0.0500
82	eePA_allwise	deg	Position angle of the error ellipse	77.7
83	Jmag_allwise	mag	J magnitude from 2MASS via the AllWISE catalogue	16.343
84	err_Jmag_allwise	mag	Error on J magnitude from 2MASS	0.158
85	Hmag_allwise	mag	H magnitude from 2MASS via the AllWISE catalogue	15.493
86	err_Hmag_allwise	mag	Error on H magnitude from 2MASS	0.188
87	Kmag_allwise	mag	K_S magnitude from 2MASS via the AllWISE catalogue	14.781
88	err_Kmag_allwise	mag	Error on K_S magnitude from 2MASS	0.122
89	ra_LSDR10	deg	Right ascension in Legacy Surveys DR10 (J2000)	1.491361150872304
90	dec_LSDR10	deg	Declination in Legacy Surveys DR10 (J2000)	–56.47533820865902
91	mag_g_LSDR10	mag	g magnitude in Legacy Surveys DR10	18.377111
92	mag_r_LSDR10	mag	r magnitude in Legacy Surveys DR10	16.903824
93	mag_i_LSDR10	mag	i magnitude in Legacy Surveys DR10	16.386793
94	mag_z_LSDR10	mag	z magnitude in Legacy Surveys DR10	16.092787
95	dered_mag_g_LSDR10	mag	Dereddened g magnitude in Legacy Surveys DR10	18.342104
96	dered_mag_r_LSDR10	mag	Dereddened r magnitude in Legacy Surveys DR10	16.880241
97	dered_mag_i_LSDR10	mag	Dereddened i magnitude in Legacy Surveys DR10	16.369452
98	dered_mag_z_LSDR10	mag	Dereddened z magnitude in Legacy Surveys DR10	16.079596
99	snr_g_LSDR10	–	Signal-to-noise ratio in the g band	536.82965
100	snr_r_LSDR10	–	Signal-to-noise ratio in the r band	1232.6284
101	snr_i_LSDR10	–	Signal-to-noise ratio in the i band	1319.4358
102	snr_z_LSDR10	–	Signal-to-noise ratio in the z band	879.1196
103	psfsize_g_LSDR10	arcsec	Weighted average PSF FWHM in the g band	1.3799053
104	psfsize_r_LSDR10	arcsec	Weighted average PSF FWHM in the r band	1.0936546
105	psfsize_i_LSDR10	arcsec	Weighted average PSF FWHM in the i band	1.0151794
106	psfsize_z_LSDR10	arcsec	Weighted average PSF FWHM in the z band	1.0915892
107	morphotype_LSDR10	–	Optical morphological classification by THE TRACTOR	SER
108	seraic_LSDR10	–	Sérsic-index value fitted/set by THE TRACTOR	5.3008156
109	L_151_WperHz	W Hz ^{–1}	K-corrected radio luminosity at 151 MHz	2.430700E27
110	err_L_151_WperHz	W Hz ^{–1}	Error on the K-corrected radio luminosity at 151 MHz	1.553722E25
111	L_1400_WperHz	W Hz ^{–1}	K-corrected radio luminosity at 1400 MHz	5.204895E26
112	err_L_1400_WperHz	W Hz ^{–1}	Error on the K-corrected radio luminosity at 1400 MHz	3.931781E25
113	linear_size_limit	–	Indicates that the linear size is an upper limit	–
114	linear_size_kpc	kpc	Linear size (via the angular size in NVSS/SUMSS)	249.0065
115	z_origin_flag	–	Flag denoting the origin of the adopted redshift	3.0
116	z_Quality_flag	–	Flag indicating the quality of the adopted redshift (1 = best)	1
117	zsp_misc	–	Miscellaneous spectroscopic redshift	0.291
118	zsp_DESI	–	Spectroscopic redshift fitted by the DESI collaboration	–
119	zsp_WARN_DESI	–	Redshift-fitting quality flag by the DESI collaboration	–
120	zph_misc	–	Miscellaneous photometric redshift	0.279
121	zph_LSDR8south	–	Photometric-redshift estimate from LS DR8 South	0.279
122	err_zph_LSDR8south	–	Error in the photometric-redshift estimate	0.027
123	zph_fclean_LSDR8south	–	Flag = 1 for sources free of blending or imaging artefacts	1
124	zph_fqual_LSDR8south	–	Flag = 1 for reliable photometric-redshift estimates	1
125	zph_ANN_wiseScos	–	Photometric redshift obtained with the ANNz framework	0.269903
126	ebv_wiseScos	mag	E(B-V), the Galactic dust extinction along the line-of-sight	0.011
127	NED_RAJ2000	deg	Fiducial right ascension in NED (J2000)	1.491445
128	NED_DEJ2000	deg	Fiducial declination in NED (J2000)	–56.4753
129	NED_type	–	Object type accompanying the alternative name in NED	G
130	z_NED	–	Fiducial redshift (spectroscopic or photometric) in NED	0.2912
131	z_ref_NED	–	Reference for the fiducial redshift in NED	20032dF...C...0000C



(a)



(b)

Figure B2. We present the P - D diagram (Section 4.1.4) as a function of (a) α_{low} and (b) α_{mid} for G4Jy-NVSS sources. These spectral indices correspond to the G4Jy_alpha and alpha_mid (i.e. G4Jy_NVSS_alpha) values in the updated G4Jy catalogue, respectively. As discussed in Appendix B, neither spectral index appears to demarcate any particular region of P - D space.

Source name	Angular size / arcmin	Redshift type	Redshift, z	Redshift reference	z _Quality_flag (Paper III)	Linear size / kpc	Reported as a GRG by
G4Jy 133	11.80	z_{sp}	0.1478	García-Pérez et al. (2024)	1	1828	Andernach et al. (2021)
G4Jy 234	6.30	z_{ph}	0.189	Duncan (2022)	5	1193	Andernach et al. (2021)
G4Jy 318	3.56	z_{ph}	0.736	Duncan (2022)	5	1556	This work
G4Jy 347	25.86	z_{sp}	0.0624	García-Pérez et al. (2024)	1	1865	Andernach et al. (2021)
G4Jy 517	38.50	z_{sp}	0.03812	Jones et al. (2009)	1	1746	Saripalli et al. (1986)
G4Jy 641	7.77	z_{sp}	0.128	White et al. (2025)	1	1070	This work
G4Jy 923	4.90	z_{sp}	0.6337	(re-fitted, Paper III)	1	2010	Bhatnagar et al. (1998)
G4Jy 1021	2.80	z_{ph}	0.931	Duncan (2022)	5	1321	This work
G4Jy 1079	14.90	z_{sp}	0.0836	García-Pérez et al. (2024)	1	1404	Machalski et al. (2007)
G4Jy 1282	19.50	z_{sp}	0.08745	DESI Collaboration et al. (2025)	1	1914	Willis & Strom (1978)
G4Jy 1525	6.10	z_{NED}	0.3462	Saripalli et al. (2005)	5	1795	Subrahmanyan et al. (1996)

Table C1. Angular sizes, redshifts, and (projected) linear sizes for 11 GRGs that are larger than 1 Mpc (Section 4.1.3). We note that angular sizes catalogued by White et al. (2020a,b) are based on NVSS and SUMSS imaging, which we revise here, based on the most-recent, available surveys. ‘Redshift type’ indicates whether the redshift is spectroscopic (z_{sp}), photometric (z_{ph}), or found through NED (z_{NED}). A guide to the assigned z _Quality_flags is provided in Section 3.2.

White et al. 2025), we estimate the linear size as 1070 kpc. We add this new GRG to Table C1 and note that the catalogued linear-size (585 kpc) is based on an outdated angular-size of 4.26 arcmin.

For **G4Jy 923**, we can precisely measure the angular size as 4.90 arcmin in VLASS. (This is only slightly above the catalogued angular-size of 4.77 arcmin.) In addition, our re-fitted spectroscopic redshift (via DESI DR1) is in perfect agreement with $z_{\text{sp}} = 0.6337$ from Bhatnagar et al. (1998). Thus, we calculate a linear size of 2010 kpc (differing from the catalogued value of 1961 kpc).

Finally, there has been considerable debate over the host galaxy of **G4Jy 1289** (see section 3.2 of Paper III), which was first considered a candidate GRG by Proctor (2016) through NVSS imaging. The MeerKAT image by Sejake et al. (2023) indicates that there are three candidates for the radio-core position: WISEA J155900.91–213935.5 (White et al. 2026), 2MASX J15590200–2140032 (Quici et al. 2025), and UGCS J155856.54–213824.3 (Andernach & Brüggén 2025). Only when the radio core, and therefore the host-galaxy identification, has been confirmed, can we obtain the correct redshift for G4Jy 1289. This would then allow us to calculate the linear size and so determine whether or not this source is a GRG (in the sense of it passing the now, more-common threshold of 700 kpc in projected linear-size).

This paper has been typeset from a $\text{\TeX}/\text{\LaTeX}$ file prepared by the author.